Progress in Oceanography 204 (2022) 102789

Contents lists available at ScienceDirect

Progress in Oceanography

journal homepage: www.elsevier.com/locate/pocean

Phytoplankton diversity emerging from chromatic adaptation and competition for light

Eva Álvarez *, Paolo Lazzari, Gianpiero Cossarini

National Institute of Oceanography and Applied Geophysics - OGS, Trieste, Italy

A B S T R A C T

The phytoplankton absorption cross-section is a fundamental quantity in biogeochemical ocean models that alters the underwater spectral light field and the photosynthetic response of phytoplankton. Phytoplankton taxa are characterized by absorption spectra with defined absorption bands in the visible region of the light spectrum that govern the capability of different taxa of phytoplankton to exploit light as a resource for growth. The interplay between the spatial and temporal gradients of underwater spectral light and the light absorption characteristics of different phytoplankton types contribute to the interactions and selection among groups and hence can be a determinant in shaping phytoplankton diversity and biogeography. In this work, we used a biogeochemical model of the Mediterranean Sea to simulate nine optically different phytoplankton functional types (PFTs) and coupled it to a radiative transfer model to simulate the spectral underwater light field where the PFTs interact. We investigated the competitive advantage provided by the different absorption spectra and the possibilities of coexistence emerging from the availability of different light habitats. By considering non-spectrally resolved optical differences among PFTs, our model results led to the dominance of *Synechococcus* sp. within picophytoplankton, coccolithophores within nanophytoplankton and dinoflagellates within microphytoplankton. By including the spectral dependency of photosynthesis, we observed how the availability of different spectral light habitats led to the coexistence of picophytoplankton groups in clear waters, whereas for nano- and microphytoplankton PFTs, the extent of coexistence permitted by light fluctuations was minimal. By combining optical and functional differences in the PFT description, we obtained PFT distributions that were in relative agreement with observed phytoplankton distributions in the Mediterranean Sea estimated from satellite and in situ high-performance liquid chromatography sampling. This result suggests that combining spectrally resolved optical traits with functional traits in the description of the autotrophic community can be a valuable tool to improve simulations of the diversity and biogeography of primary producers in the ocean.

1. Introduction

Phytoplankton are a key compartment in the biochemistry of the ocean. They assimilate inorganic nutrients and fix carbon by photosynthesis, and thus, they are important in the coupling between nutrients and the carbon cycle (Buesseler, 1998). Phytoplankton community composition is an emerging property resulting from the interaction, competition and selection of phytoplankton taxa. The relative fitness of different phytoplankton types is determined by several traits, including their growth dependence on resource availability as well as their susceptibility to predation and other causes of mortality. Differences in traits among phytoplankton types may contribute to their interactions and selection in the physical, chemical and predatory environments and hence to their spatial and temporal distributions.

One fundamental trait affecting phytoplankton growth is the light absorption cross-section of the cells. Photochemical reactions are powered by light, and the absorbed amount depends on the available irradiance and on the amount of light absorbed by the phytoplankton cells. The phytoplankton absorption cross-section is a fundamental quantity in physical and biogeochemical ocean models that alters the underwater spectral light transmission and the photosynthetic response of phytoplankton to available light. Algal pigments have defined absorption bands in the visible region of the electromagnetic spectrum (Bidigare et al., 1990; Bricaud et al., 2004), and different phytoplankton groups are characterized by different pigment suites (Sathyendranath et al., 1987). Thus, light absorption coefficients are wavelength-dependent (i.e., colour-dependent) and allow the species to exploit environmental variation in spectral light by employing different photosynthetic pigments that absorb different colours of light.

Therefore, underwater light is not a single resource for phytoplankton; rather, it offers a spectrum of resources. Underwater irradiance spectra are generated by the wavelength-dependent absorption and scattering of light by water, dissolved material and particulate material. Hence, the spectrum of photosynthetically available radiation varies seasonally, latitudinally and as it penetrates the water column. Competition theory started treating light as a single resource (Huisman and Weissing, 1995, 1994) and predicted that the best competitor for light would outcompete other phytoplankton types (Huisman et al.,

* Corresponding author.
E-mail address: ealvarez@ogs.it (E. Álvarez).

https://doi.org/10.1016/j.pocean.2022.102789
Received 26 April 2021; Received in revised form 21 March 2022; Accepted 31 March 2022
Available online 4 April 2022

1999). When competition models were extended by incorporating the full spectrum of light, it was observed that groups with very similar absorption spectra faced stronger competition for light, and species that absorbed different parts of the light spectrum were able to coexist (Burson et al., 2019; Stomp et al., 2007, 2004). This result indicated that the spectral light absorption characteristics of different phytoplankton types used to exploit light resources are important in determining species selection in the spectral light gradient. Hence, changes in water colour may shift the competitive interactions between phytoplankton species that differ in pigment composition and considerably affect their spatial and temporal distributions.

Biogeochemical models that include the spectral aspect of light (e.g., Baird et al., 2016; Dutkiewicz et al., 2015; Gregg and Rousseaux, 2017; Xiu and Chai, 2014) are valuable tools that can be used to explore the dynamics of competition for light in the ocean. These models simulate a variety of light habitats in relation to the fluctuations in space and time of the magnitude and spectral composition of light. By describing the variability of light-harvesting traits in phytoplankton, such models show the role of the spectral composition of in situ irradiance and light absorption coefficients in shaping habitats for small phytoplankton in oligotrophic waters (Hickman et al., 2010) and in the global ocean (Holtrop et al., 2021). What has not been addressed in previous works, to the best of our knowledge, is the capability of spectral light absorption traits to discriminate the distribution of the whole phytoplankton community in any particular area of the ocean. Previous studies focused only on picoplankton taxa (Burson et al., 2019; Stomp et al., 2007, 2004), considering the influence of light harvesting traits combined with temperature and nutrient uptake traits on shaping habitats for small phytoplankton (Hickman et al., 2010). Holtrop et al. (2021) did not consider differences in growth among picophytoplankton types. Throughout this work, we explored the role of the underwater light spectrum as a major selective factor in the natural phytoplankton community of the Mediterranean Sea. With this aim, we considered a comprehensive description of the light absorption traits of the phytoplankton found in the area and assessed differences in growth among phytoplankton types resulting from variability in spectral light absorption traits.

The Mediterranean Sea is a mid-latitude sea almost completely enclosed by land. It is an optically complex basin that exhibits a variety of light conditions, from clear to turbid waters (D'Alimonte et al., 2003). Several reasons have been reported to explain its particular optical properties, including a high contribution of coloured dissolved organic matter (CDOM) (Organelli et al., 2014), particular pigment ratios in the phytoplankton community (Organelli et al., 2011), the abundance of small coccolithophores (Gitelson et al., 1996) and the influence of Saharan dust (Claustre et al., 2002). Although primary production annual budgets are overall low and the dominance of picophytoplankton seems generalized (Siokou-Frangou et al., 2010), observations indicate a longitudinal gradient in productivity, with the eastern Mediterranean being more oligotrophic than the western Mediterranean (Bosc et al., 2004; Turley et al., 2000). In areas of higher nutrient availability, cyanobacteria and picoeukaryotes often coexist or alternate with diatoms, dinoflagellates and other flagellates. Phytoplankton populations dominated by different functional groups and species alternate during the seasonal cycle and populate the deep chlorophyll maximum. Generally, basins have been intensively studied to delineate the biogeographic distribution of phytoplankton functional types (PFTs). Regional-specific satellite products that resolve several phytoplankton groups and size classes are available (DiCicco et al., 2017; Volpe et al., 2019), as are field observations of phytoplankton pigment concentrations by high-performance liquid chromatography (HPLC). Altogether, the Mediterranean Sea constitutes a suitable laboratory to explore the influence of chromatic adaptation of the whole phytoplankton community as a result of the competition for light.

The biogeochemical flux model (BFM) resolves the biogeochemistry of the Mediterranean Sea (Vichi et al., 2007) and has been used in a variety of applications (e.g., Lazzari et al., 2012; Salon et al., 2019). To use this modelling framework to explore competition for spectral light, three elements were combined in this work: i) the inclusion of a radiative transfer model to simulate realistic underwater spectral light observed in the area of study; ii) the definition of a light-harvesting trait that gives the competitive advantage and its variability on the phytoplankton taxa found in the area; and iii) the control on other phytoplankton traits and phytoplankton mortality that permitted us to observe the result of competition for light. The first two elements were solved by employing a radiative transfer model that was coupled to BFM (Lazzari et al., 2021a; Terzić et al., 2021) and described the propagation of light through water being absorbed and scattered by optically active constituents, namely, water, CDOM, detritus and phytoplankton. The phytoplankton community was described by several PFTs intended to cover the whole autotrophic community of the basin and to capture most of their variability in optical properties. Hence, the selected PFTs are somehow relevant in the Mediterranean Sea phytoplankton community (Siokou-Frangou et al., 2010), and their distributions can be compared to independent field observations.

The result of competition for a particular resource among phytoplankton groups, e.g., light in this case, and how it affects PFT relative density will inevitably be dependent on the trophic interactions of such groups. Given that the PFTs described in the model share common predators, simulated phytoplankton community structure, diversity and dynamics will be affected by the zooplankton community response and the grazing formulation (Anderson et al., 2010; Prowe et al., 2012). Two species are in competition whenever the presence of either species leads to a reduced population density for the other species at equilibrium. This interaction can be direct if the two species compete directly; they are indirectly linked through the food web or indirectly linked when they share predators. Such indirect interactions are known as apparent competition resulting from shared predation (Holt, 1977). Predator-mediated apparent competition may place constraints on the kind and number of prey species that can coexist in the system. Instead of just removing zooplankton from the system, which would make model simulations not comparable to field observations, we used different grazing formulations as a tool to induce different levels of competition among phytoplankton (Holt, 1977; Vallina et al., 2014).

Multiple prey functional responses are classified according to whether the preferences of a given grazer for their prey are constant or density-dependent (i.e., no-switching vs. switching) (Anderson et al., 2010; Gentleman et al., 2003). Active-switching formulations make the grazer feed comparatively more on the more abundant prey, and grazing pressure decreases as prey becomes scarcer, which stabilizes the system and promotes the coexistence of different prey types. Regarding competition for light, this means that even if one PFT is a better competitor in terms of absorbing different light colours of the spectrum, all the other PFTs can coexist. Hence, an active-switching grazing formulation maximizes the variability of optical properties found in the phytoplankton community. Alternatively, no-switching formulations make the predator graze a constant proportion of each prey, destabilizing the system and leading to competitive exclusion. Regarding competition for light, this means that under light limitation, the most competitive PFT will be the one with the highest absorbed irradiance that reflects the better match of its absorbing traits to the incoming spectral light. With a no-switching grazing formulation, a single PFT would dominate the community under each particular light habitat, and opportunities for coexistence would arise from the variability in the spectral composition of light.

This is the first time a 3D biogeochemical model with a radiative transfer component and with such complexity in terms of PFTs has been proposed for the Mediterranean Sea. By including the novel components of the BFM model (i.e., bio-optical coupling and optically different PFTs) and the presence of zooplankton, this modelling framework provides a reasonable level of complexity to be used as a virtual laboratory to investigate light competition in a pelagic ecosystem. Particularly, we

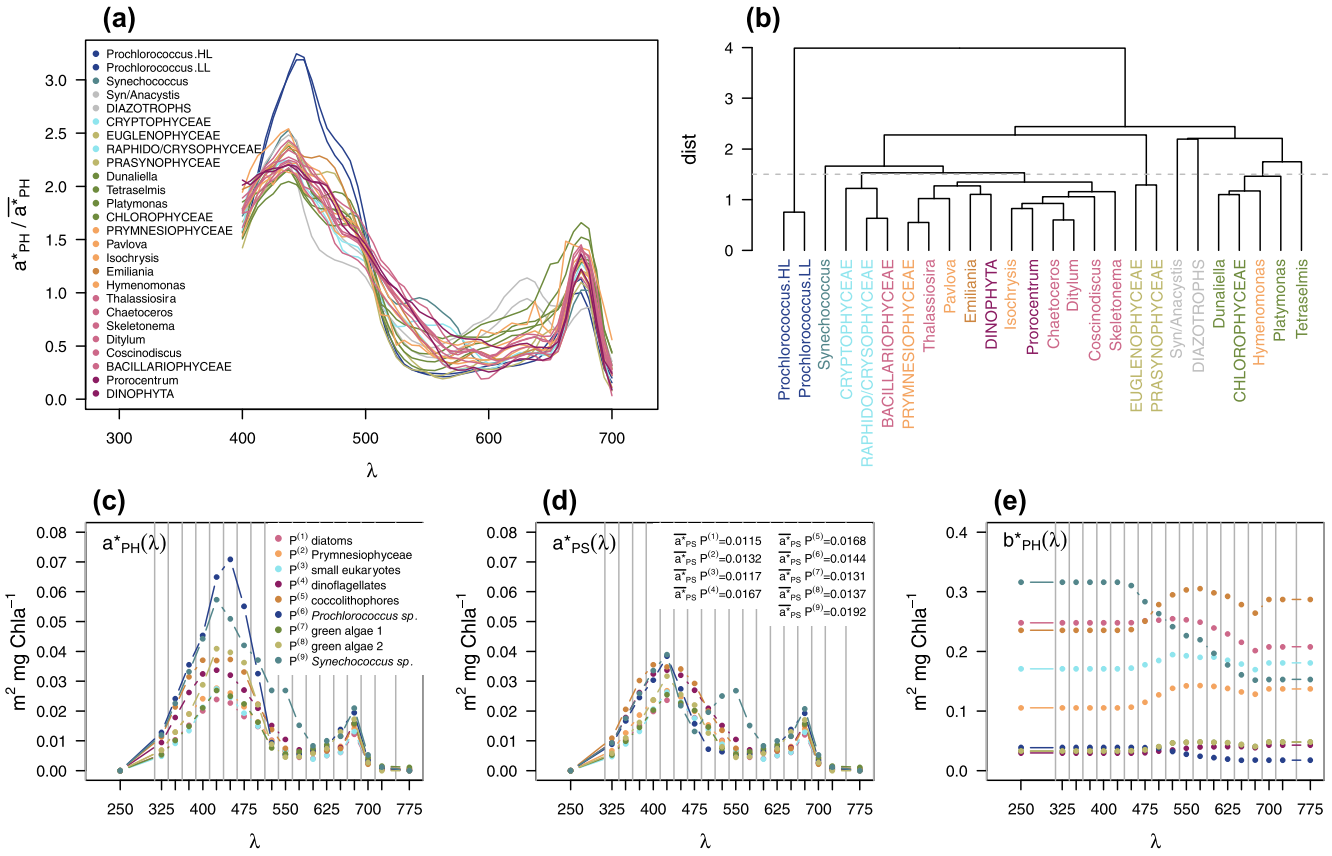

Fig. 1. Phytoplankton chlorophyll-specific absorption spectra **(a)** digitized from the literature in 6.5-nm intervals and normalized by the mean between 400 and 700 nm. Each line represents an averaged spectrum belonging to the same phytoplankton genus (indicated by the genus name) or higher taxonomic rank (in capitals); **(b)** dendrogram after hierarchical cluster analysis on the 26 $a^*_{PH}(\lambda)$ spectra; spectra for each of the 9 PFTs proposed in terms of **(c)** $a^*_{PH}(\lambda)$, **(d)** $a^*_{PS}(\lambda)$ and **(e)** $b^*_{PH}(\lambda)$. Grey vertical lines indicate the extremes of the wavebands, and the points indicate the averaged coefficients for each waveband used in the model. The values inserted in panel d show the value of $\overline{a^*_{PS}}$ for each PFT.

will focus on investigating which phytoplankton groups succeed in terms of competition for light under the relatively ample and variable range of light conditions of the basin, to what extent the availability of different spectral light habitats permit the coexistence of phytoplankton types, and eventually, determine whether the complexity of our approach is adequate to simulate the spectral light conditions under which all PFTs observed in the area of study can succeed.

The structure of the rest of this paper is as follows. In section 2, we analyse the optical properties of the phytoplankton community found in the Mediterranean Sea, describe the radiative transfer and biogeochemical models, and collect observations about PFT distribution in the Mediterranean Sea. In section 3, model outcomes are used to analyse competition for light among PFTs and evaluate light niche distribution. We explored the effect of increased physiological differentiation among the PFTs and observed the simulated PFT distributions in the Mediterranean Sea compared to field observations in the basin. Finally, in section 4, we discuss the relevance of including spectral light-dependent physiology in the lower trophic levels of biogeochemical models. We also foresee some potential future directions to integrate spectral optical properties with other physiological and ecological characteristics.

2. Materials and methods

2.1. Phytoplankton optical properties

To assess how many and which types of optically different phytoplankton groups can represent most of the variability in optical properties observed in nature, we performed a review of the literature reporting the optical properties of different phytoplankton taxa (Ahn et al., 1992; Bricaud et al., 1988; Clementson and Wojtasiewicz, 2019; Dubinsky et al., 1986; Dupouy et al., 2008; Fujiki and Taguchi, 2002; Johnsen and Sakshaug, 2007; Kishino et al., 1985; Lorenzo et al., 2019; Lutz et al., 2001; Mao et al., 2010; Metsamaa et al., 2006; Mitchell and Kiefer, 1988; Moore et al., 1995; Moore and Chisholm, 1999; Morel et al., 1993; Morel and Bricaud, 1981; Nair, 2007; Proctor and Roesler, 2010; Staehr et al., 2002; Stramski and Morel, 1990; Subramaniam et al., 1999; Suggett et al., 2007; Whitmire et al., 2010; Wojtasiewicz and Stoń-Egiert, 2016; Zhou et al., 2012). All references provided chlorophyll-specific absorption and scatter coefficients and backscatter to scatter ratios for phytoplankton growing in culture under different conditions of light, nutrient supply and temperature. All curves were digitized in R 4.0.0 (R Core Team, 2020) using the package *digitize* version 0.0.4 (Poisot, 2011). The complete dataset is provided as supplementary data and is fully described in Appendix A.

A total of 177 chlorophyll-specific absorption spectra ($a^*_{PH}(\lambda)$) were used to discriminate optically different phytoplankton groups. Different growth conditions provoke significant changes in cellular pigment concentrations and thus in the light absorption features, but the spectral absorption signature of a given phytoplankton species tends to be recognizable despite intraspecific variability (Organelli et al., 2017). To minimize the effect of different growth conditions, we averaged spectra belonging to the same phytoplankton taxa. This resulted in 26 $a^*_{PH}(\lambda)$ spectra that were normalized by the mean between 400 and 700 nm (Fig. 1**a**). This normalization step ensured that any difference between spectra would be related to their spectral distribution and not to their absolute magnitude.

Table 1
Proposed optically different phytoplankton functional types (PFTs), size classes to which they are assigned (PSCs), operational descriptions, comparable groups determined from diagnostic pigments [1](DiCicco et al., 2017) and relevance of equivalent PFTs in the Mediterranean Sea [2](Siokou-Frangou et al., 2010).

Name in BFM	PFT	PSC	Definition	Comparable group by DP[1]	Relevance[2]
$P^{(9)}$	*Synechococcus* sp.	pico	red cyanobacteria	Prokar	2–75.7 %
$P^{(6)}$	*Prochlorococcus* sp.	pico	green cyanobacteria	Prokar & Green	
$P^{(3)}$	small eukaryotes	pico	Cryptophyceae, Pelagophyceae & Chrysophyceae	Crypto	Cryptophyceae 5.2–11.7 % Pelagophyceae 4–33.8 %
$P^{(7)}$	green algae 1	nano	Chlorophyceae	Green	5.3–21 %
$P^{(8)}$	green algae 2	nano	Prasinophyceae & Euglenophyceae	Green	
$P^{(2)}$	Prymnesiophyceae	nano	non-calcifiying Haptophyta	Hapto	31.8–51 % (includes Chrysophyceae)
$P^{(5)}$	coccolithophores	nano	calcifiying Haptophyta	Hapto	
$P^{(1)}$	Bacillariophyceae	micro	silifiers	Diatoms	3.4 – 76 %
$P^{(4)}$	dinoflagellates	micro	large phyto non-silifiers	Dinophytes	4 – 43.8 %
–	diazotrophs	–	N_2-fixers	–	negligible
–	*Syn/Anacystis* sp.	–	chroococcales cyanobacteria	–	negligible

The resultant 26 spectra were classified by applying agglomerative hierarchical clustering through the *agnes* function from the R package *cluster* version 2.1.0 (Maechler et al., 2019). The dendrogram was obtained using the complete linkage method, and the Euclidean distance was chosen as the criterion for evaluating the similarity level. According to the similarity level of the clustering, we separated groups for *Prochlorococcus* sp.; two groups of green algae; *Synechococcus* sp.; small eukaryotes that included Crypto-, Pelago- and Chrysophyceae; and brown algae (Fig. 1**b**). While the clustering analysis classified brown algae as an optical homogeneous group, it included functionally diverse groups. Thus, we decided to split brown algae into Haptophyta, both calcifying (coccolithophores) and noncalcifying, and microphytoplankton, both silicifying (diatoms) and non-silicifying (dinoflagellates). One group that included diazotrophs and the genera *Synechocystis* sp. and *Anacystis* sp. was also separated according to the clustering analysis, but these species are negligible in the Mediterranean Sea. Therefore, a total of nine optically different phytoplankton groups (Table 1) were proposed to be included in the ecosystem model as nine phytoplankton functional types (PFTs): $P^{(1)}$ (diatoms), $P^{(2)}$ (non-calcifying Haptophyta or Prymnesiophyceae), $P^{(3)}$ (small eukaryotes), $P^{(4)}$ (dinoflagellates), $P^{(5)}$ (calcifying Haptophyta or coccolithophores), $P^{(6)}$ (*Prochlorococcus* sp.) $P^{(7)}$ (Eugleno- and Prasinophyceae), $P^{(8)}$ (Chlorophyceae) and $P^{(9)}$ (*Synechococcus* sp.) (Fig. 1**c**).

Absorption spectra for photosynthetic pigments ($a^*_{PS}(\lambda)$) were computed following the spectral reconstruction technique (Babin et al., 1996; Bidigare et al., 1990; Hickman et al., 2010). This technique adjusts the total absorption spectrum by the wavelength-dependent ratio of light absorption by non-photosynthetic pigments to total pigments. To obtain the relative pigment concentrations for the reconstructions, we first assigned one set of four pigment types to each PFT. All PFTs shared chlorophyll *a* (Chl-a), photosynthetic carotenoids (PSC) and non-photosynthetic carotenoids (PPC); the fourth was phycoerythrin (PEB) for *Synechococcus* sp., chlorophyll *b* (Chl-b) for green algae and *Prochlorococcus* sp., and chlorophyll *c* (Chl-c) for the rest. We scaled the weight-specific absorption spectra for the pigment types (Bidigare et al., 1990) to yield the lowest sum of residuals between the reconstructed $a^*_{PH}(\lambda)$ spectrum and the measured $a^*_{PH}(\lambda)$ spectrum (Hickman et al., 2010). $a^*_{PS}(\lambda)$ was reconstructed with the weight-specific absorption spectra and the relative pigment concentrations of photosynthetic pigments (Fig. 1**d**). The average $a^*_{PS}(\lambda)$ from 387.5 to 712.5 nm constitutes the average absorption cross-section for photochemistry ($\overline{a^*_{PS}}$, m^2 mg Chl^{-1}). The value of $\overline{a^*_{PS}}$ for each PFT is shown in Fig. 1**d**.

Finally, 36 chlorophyll-specific scatter spectra ($b^*_{PH}(\lambda)$) were averaged for the 9 PFTs (Fig. 1**e**), and from 35 backscatter to total scatter ratio spectra ($br_{PH}(\lambda)$), mean non-spectral backscatter ratios were computed for each PFT (Table 2).

2.2. Modelling framework

The biogeochemical flux model (BFM) resolves the cycling of carbon, nitrogen, phosphorus and silica in the ocean through inorganic, dissolved and particulate organic components, as described in Vichi et al. (2007). The living components are phytoplankton (P), heterotrophic bacteria (B) and grazers (Z); the non-living organic components are dissolved and particulate organic matter (R); and the inorganic components are nutrients (N) and dissolved gases (O) (Fig. 2**a**). A superscript appended to the component name indicates different types of the same component; thus, PFTs are labelled consecutively from $P^{(1)}$ to $P^{(9)}$, grazers from $Z^{(3)}$ to $Z^{(6)}$, bacteria as $B^{(1)}$, dissolved organic matter as $R^{(1)}$ to $R^{(3)}$ and non-algal particulate organic carbon as $R^{(6)}$. The subscript appended to each component type indicates the elemental constituents among carbon (C), nitrogen (N), phosphorus (P) and chlorophyll (Chl) for phytoplankton, silica (Si) for diatoms and coloured fraction (l) for dissolved organic matter. For example, $P^{(1)}_C$ represents the carbon content of PFT number 1, and $R^{(2)}_l$ represents the coloured carbon content of the semi-labile dissolved organic matter. For rates, the subscript indicates the component (P, Z and B), and the superscript indicates the specific type. Therefore, as an example, the photosynthetic rate of diatoms ($P^{(1)}$) is denoted as $photosynthesis^{(1)}_P$, and the exudation rate of microzooplankton ($Z^{(3)}$) is denoted as $exudation^{(3)}_Z$. For parameters, the notation is the same as for rates, with the exception that the subscript indicates the component they apply among all phytoplankton pigments (PH), photosynthetic pigments (PS), zooplankton (Z), bacteria (B), non-algal particles (NAP), coloured dissolved carbon (CDOM) and water (W).

In this section, we first describe the radiative transfer model that resolves the penetration of spectral irradiance in the water column and its interaction with optically active constituents (Section 2.2.1); next, we describe the novel BFM configuration with 9 PFTs, CDOM and NAP as optically active components and the dynamical equations governing their changes in mass (Section 2.2.2). Finally, we describe the set of model simulations performed to assess the prevalence and distribution of optically different PFTs in the spectral light habitats available (Section 2.2.3).

2.2.1. Bio-optical model

A radiative transfer model has been coupled to the BFM (Terzić et al., 2021) to resolve the penetration of spectral irradiance, as it is absorbed and scattered within the water column by the components that are optically active (blue shadowed in Fig. 2**a**). The radiative transfer model coupled to the BFM allows us to simulate a virtual environment where the spectral underwater light field is affected by the optical properties of 9 PFTs, CDOM and non-algal particles (NAPs). Spectral irradiance at the ocean surface is derived from the Ocean Atmosphere Spectral Irradiance Model (OASIM) (Gregg and Casey, 2009) coupled to the European Centre for Medium-Range Weather Forecasts (ECMWF) model (Lazzari et al., 2021b). It provides direct and diffuse components of incoming

Table 2
Parameters of the bio-optical component.

Parameter	Description	Value	Units	Source
r_d	E_d-specific scattering coefficient	1.0	–	(Aas, 1987)
r_s	E_s-specific scattering coefficient	1.5	–	(Aas, 1987)
r_u	E_u-specific scattering coefficient	3.0	–	(Aas, 1987)
υ_s	average cosine E_s stream	0.83	–	(Aas, 1987)
υ_u	average cosine E_u stream	0.4	–	(Aas, 1987)
$a_W(\lambda)$	absorption coefficients of seawater	in Fig. 2b	m^{-1}	(Pope and Fry, 1997)
$b_W(\lambda)$	scatter coefficients of seawater	in Fig. 2b	m^{-1}	(Smith and Baker, 1981)
br_W	backscatter to total scatter ratio of seawater	0.5	–	(Morel, 1974)
c_{CDOM} (450)	CDOM mass-specific absorption coefficient at 450 nm	0.015	m^2 mgC^{-1}	(Dutkiewicz et al., 2015)
S_{CDOM}	CDOM absorption spectral slope	0.017	nm^{-1}	(Kitidis et al., 2006)
$a^*_{CDOM}(\lambda)$	mass-specific absorption coefficients of CDOM	in Fig. 2c	m^2 mgC^{-1}	
c_{NAP} (440)	NAPs mass-specific absorption coefficient at 440 nm	1.33e-3	m^2 mgC^{-1}	(Dutkiewicz et al., 2015)
S_{NAP}	NAPs absorption spectral slope	0.013	nm^{-1}	(Gallegos et al., 2011)
$a^*_{NAP}(\lambda)$	mass-specific absorption coefficients of NAPs	in Fig. 2d	m^2 mgC^{-1}	
d_{NAP} (550)	NAPs mass-specific scatter coefficient at 550 nm	0.029	m^2 mgC^{-1}	(Dutkiewicz et al., 2015)
e_{NAP}	NAPs exponent for scatter	0.5	–	(Gallegos et al., 2011)
$b^*_{NAP}(\lambda)$	mass-specific scatter coefficients of NAPs	in Fig. 2d	m^2 mgC^{-1}	
br_{NAP}	backscatter to total scatter ratio of NAPs	0.005	–	(Gallegos et al., 2011)
$a^*_{PH}(\lambda)$	chl-specific absorption coefficients of total pigments	in Fig. 1c	m^2 $mgChl^{-1}$	Appendix A
$a^*_{PS}(\lambda)$	chl-specific absorption coefficients of photosynthetic pigments	in Fig. 1d	m^2 $mgChl^{-1}$	Appendix A
$b^*_{PH}(\lambda)$	chl-specific scatter coefficients of phytoplankton	in Fig. 1e	m^2 $mgChl^{-1}$	Appendix A
$br^{(1)}_{PH}$	backscatter to total scatter ratio of $P^{(1)}$	0.088	–	Appendix A
$br^{(2)}_{PH}$	backscatter to total scatter ratio of $P^{(2)}$	0.038	–	Appendix A
$br^{(3)}_{PH}$	backscatter to total scatter ratio of $P^{(3)}$	0.061	–	Appendix A
$br^{(4)}_{PH}$	backscatter to total scatter ratio of $P^{(4)}$	0.043	–	Appendix A
$br^{(5)}_{PH}$	backscatter to total scatter ratio of $P^{(5)}$	0.076	–	Appendix A
$br^{(6)}_{PH}$	backscatter to total scatter ratio of $P^{(16)}$	0.118	–	Appendix A
$br^{(7)}_{PH}$	backscatter to total scatter ratio of $P^{(7)}$	0.103	–	Appendix A
$br^{(8)}_{PH}$	backscatter to total scatter ratio of $P^{(8)}$	0.118	–	Appendix A
$br^{(9)}_{PH}$	backscatter to total scatter ratio of $P^{(9)}$	0.118	–	Appendix A
f_{CDOM}	fraction of CDOM in the exuded DOM	0.02	–	(Dutkiewicz et al., 2015)
l_{CDOM}	maximum photobleaching rate of CDOM	0.167	d^{-1}	(Dutkiewicz et al., 2015)
I_{CDOM}	threshold for maximum photobleaching rate of CDOM	5.2e6	µmol quanta m^{-2} d^{-1}	(Dutkiewicz et al., 2015)
Q^C_{10}	Q_{10} value for CDOM remineralization	2.95	–	
d_{CDOM}	remineralization rate of recalcitrant CDOM at 10 °C	3e-5	d^{-1}	

light at the ocean surface in 33 wavebands between 187.5 and 4000 nm. The penetration of light in the ocean is resolved in the full set of wavebands, but for the purpose of this work, we will focus on the 19 wavebands covering the range from 187.5 to 800 nm (the widths of the wavebands are indicated as vertical lines in Fig. 1**c-e and b-d**). Parameter values concerning the radiative transfer component are presented in Table 2.

The vertical change in irradiance is described with three state variables, all in W m^{-2}: downwelling direct ($E_d(\lambda)$) and diffuse ($E_s(\lambda)$) components and an upward diffuse component ($E_u(\lambda)$), and solving this system of differential equations (Aas, 1987; Ackleson et al., 1994; Gregg, 2002):

$$dE_d(\lambda)/dz = -\frac{a(\lambda)+b(\lambda)}{\upsilon_d}\times E_d(\lambda) \quad (1)$$

$$dE_s(\lambda)/dz = -\frac{a(\lambda)+r_s\times bb(\lambda)}{\upsilon_s}\times E_s(\lambda)+\frac{r_u\times bb(\lambda)}{\upsilon_u} \times E_u(\lambda)+\frac{b(\lambda)-r_d\times bb(\lambda)}{\upsilon_d}\times E_d(\lambda) \quad (2)$$

$$-dE_u(\lambda)/dz = -\frac{a(\lambda)+r_u\times bb(\lambda)}{\upsilon_u}\times E_u(\lambda)+\frac{r_s\times bb(\lambda)}{\upsilon_s} \times E_s(\lambda)+\frac{r_d\times bb(\lambda)}{\upsilon_d}\times E_d(\lambda) \quad (3)$$

where $a(\lambda)$ is the total absorption, $b(\lambda)$ is the total scatter, and $bb(\lambda)$ is the backward scatter, all in m^{-1}. r_s, r_u and r_d are the effective scattering coefficients, and υ_d, υ_s and υ_u are the average cosines of the three streams, which are constant for diffuse radiance but vary with solar zenith angle for direct radiance. For details on the derivation of the solution see Terzić et al. (2021).

Total $a(\lambda)$, $b(\lambda)$ and $bb(\lambda)$ depend on the additive contribution of seawater and the biogeochemical constituents along the water column (asterisk indicates mass specific quantities). Total $a(\lambda)$ is calculated from the attenuation by water ($a_W(\lambda)$, m^{-1}, Pope and Fry (1997), Fig. 2**b**), CDOM ($a_{CDOM}(\lambda)$, m^{-1}), NAP ($a_{NAP}(\lambda)$, m^{-1}) and phytoplankton ($a_{PH}(\lambda)$, m^{-1}).

$$a(\lambda) = a_W(\lambda)+a_{NAP}(\lambda)+a_{CDOM}(\lambda)+a_{PH}(\lambda) \quad (4)$$

For CDOM, $a_{CDOM}(\lambda)$ is the product of total CDOM biomass ($R^{(1)}_l$, $R^{(2)}_l$ and $R^{(3)}_l$, mgC m^{-3}) and the mass-specific absorption coefficients ($a^*_{CDOM}(\lambda)$, m^2 mgC^{-1}). $a^*_{CDOM}(\lambda)$ is an exponential function of wavelength with a spectral slope (S_{CDOM}) of 0.017 nm^{-1} and a mass-specific

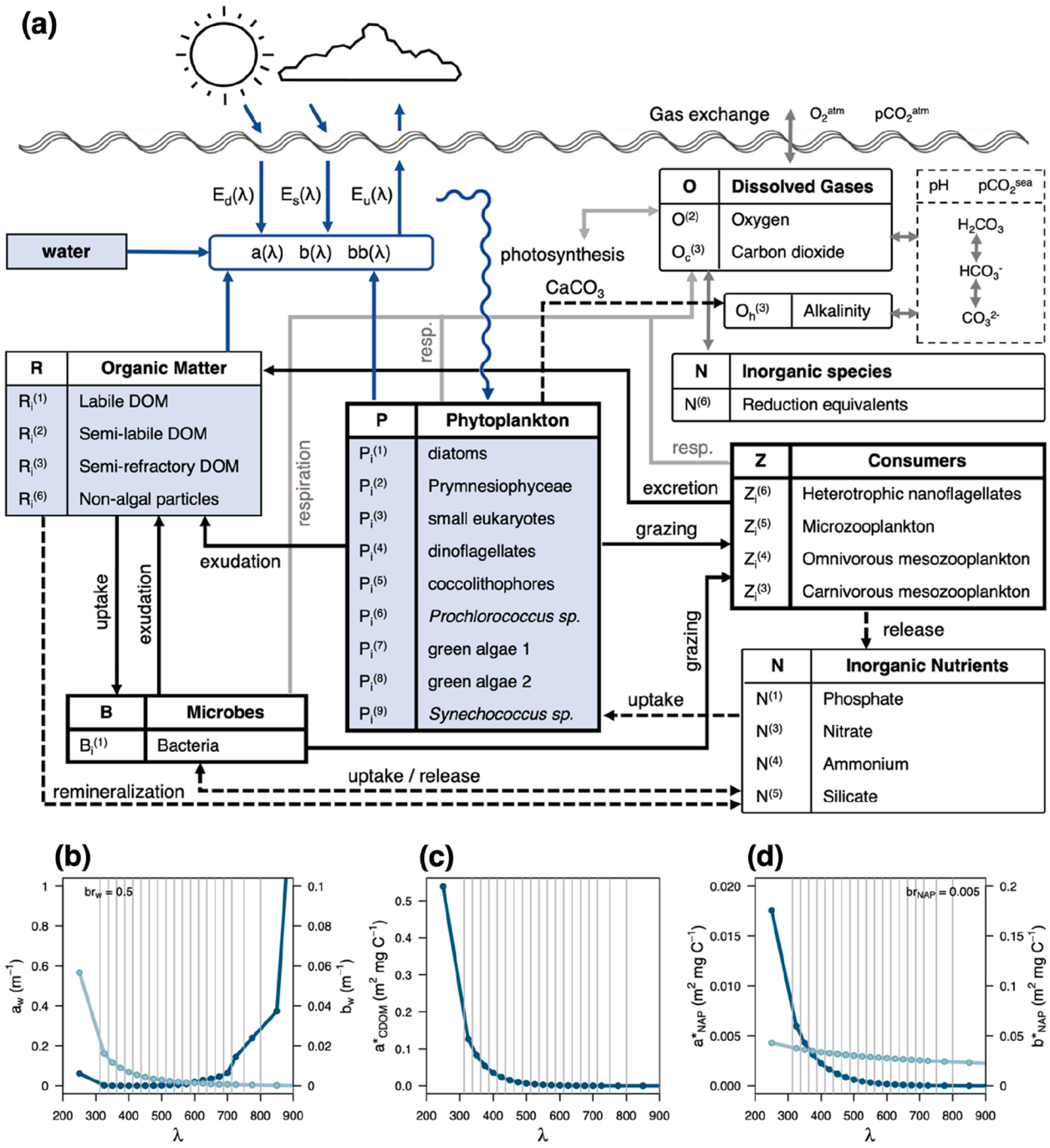

Fig. 2. **(a)** Bio-optical module (in blue) coupled to the BFM (greyscale); blue shadowed boxes highlight the optically active constituents. Absorption (dark blue, left axis) and scatter (light blue, right axis) spectra of **(b)** water, **(c)** CDOM and **(d)** non-algal particles. Grey vertical lines indicate the extremes of the wavebands, and the dots indicate the values used in the model, which are averaged integrals over the wavebands.

absorption (c_{CDOM}) of 0.015 m^2 mgC^{-1} at 450 nm (Fig. 2**c**).

$$a_{CDOM}(\lambda) = a^*_{CDOM}(\lambda) \times \left(R_l^{(1)} + R_l^{(2)} + R_l^{(3)}\right) = c_{CDOM}(450) \times exp[-S_{CDOM} \times (\lambda - 450)] \times \left(R_l^{(1)} + R_l^{(2)} + R_l^{(3)}\right) \quad (5)$$

Similarly, for NAP, $a_{NAP}(\lambda)$ is the product of the biomass of non-algal particles ($R_C^{(6)}$, mgC m^{-3}) and the mass-specific absorption coefficients ($a^*_{NAP}(\lambda)$, m^2 mgC^{-1}), which are an exponential function of wavelength with a spectral slope (S_{NAP}) of 0.013 and a reference absorption (c_{NAP}) of 1.33e-3 m^2 mgC^{-1} at 440 nm (Gallegos et al., 2011) (Fig. 2**d**).

$$a_{NAP}(\lambda) = a^*_{NAP}(\lambda) \times R_C^{(6)} = c_{NAP}(440) \times exp[-S_{NAP} \times (\lambda - 440)] \times R_C^{(6)} \quad (6)$$

For phytoplankton, $a_{PH}(\lambda)$ is the sum of the contribution of all PFTs, each contributing with its chlorophyll ($P_{Chl}^{(i)}$, mgChla m^{-3}) times the chlorophyll-specific absorption coefficients of all phytoplankton pigments ($a^*_{PH}(\lambda)$, m^2 mgChla^{-1}, Fig. 1**c**):

$$a_{PH}(\lambda) = \sum_{i=1}^{9} a^{*(i)}_{PH}(\lambda) \times P_{Chl}^{(i)} \quad (7)$$

Total $b(\lambda)$ is calculated from the scatter of water ($b_W(\lambda)$, m^{-1}, Smith

and Baker (1981), Fig. 2**b)**, NAP ($b_{NAP}(\lambda)$, m^{-1}) and phytoplankton ($b_{PH}(\lambda)$, m^{-1}).

$$b(\lambda) = b_W(\lambda) + b_{NAP}(\lambda) + b_{PH}(\lambda) \quad (8)$$

NAPs scatter light proportionally to their biomass and their mass-specific coefficients ($b^*_{NAP}(\lambda)$, m^2 mgC^{-1}), which are a power law function of wavelength with an exponent (e_{NAP}) of 0.5 and a reference scatter (d_{NAP}) of 0.029 m^2 mgC^{-1} at 550 nm (Gallegos et al., 2011) (Fig. 2**d)**.

$$b_{NAP}(\lambda) = b^*_{NAP}(\lambda) \times R^{(6)}_C = d_{NAP}(550) \times (550/\lambda)^{eNAP} \times R^{(6)}_C \quad (9)$$

For phytoplankton, $b_{PH}(\lambda)$ is the sum over all PFTs, each contributing with its chlorophyll concentration multiplied by its chlorophyll-specific scattering coefficients ($b^*_{PH}(\lambda)$, m^2 $mgChla^{-1}$, Fig. 1**e**).

$$b_{PH}(\lambda) = \sum_{i=1}^{9} b^{*(i)}_{PH}(\lambda) \times P^{(i)}_{Chl} \quad (10)$$

We have not considered any wavelength dependency on the total scatter to backward scatter ratio for any of the constituents; hence, total backscatter ($bb(\lambda)$) is computed in all cases as the total scatter multiplied by a constant backscattering to total scattering ratio, that is, 0.5 for water (Morel, 1974) and 0.05 for NAP (Gallegos et al., 2011), and it ranges between 0.038 and 0.118 for phytoplankton ($br^{(i)}_{PH}$) (Table 2).

$$bb(\lambda) = b_W(\lambda) \times br_W + b_{NAP}(\lambda) \times br_{NAP} + \sum_{i=1}^{9} b^{*(i)}_{PH}(\lambda) \times P^{(i)}_{Chl} \times br^{(i)}_{PH} \quad (11)$$

Once the system is solved for each depth layer (z), the total scalar irradiance at each layer is computed by scaling those three streams by their inverse average cosines. $E_0(\lambda)$ is the total scalar irradiance per day converted to quanta (μmol quanta m^{-2} d^{-1}) and represents the available light for biogeochemical processes in the water column, e.g., phytoplankton growth and consequently photoacclimation. The integral value of $E_0(\lambda)$ from 387.5 to 800 nm is considered the total light that degrades CDOM.

$$E_0(\lambda) = [E_d(\lambda)/\upsilon_d + E_s(\lambda)/\upsilon_s + E_u(\lambda)/\upsilon_u] \times (\lambda \times 8.36 \bullet 10^{-3}) \times 86400 \quad (12)$$

$$PAR = \int_{387.5}^{800} E_0(\lambda) d\lambda \quad (13)$$

2.2.2. Biogeochemical model

The modular structure of the BFM allows an increase in the number of living functional types starting from the standard BFM configuration (Vichi et al., 2015). Most applications of the BFM use four PFTs based on a size subdivision in three size classes (micro, nano and picophytoplankton) and a functional description that distinguishes dinoflagellates and diatoms within the microphytoplankton (Vichi et al., 2015; Lazzari et al., 2012).

To cover the observed variability in phytoplankton optical properties, we propose a novel configuration of BFM with nine PFTs. The nine PFTs are conventionally subdivided into three size class groups (PSCs, Table 1). As the reference configuration for the present work, the PFTs are clones considering their functional and optical characteristics and their trophic interactions within a given PSC, and the standard BFM configurations of each PSC are used (Vichi et al., 2015). Thus, three PFTs share the same physiological characteristics as the former picophytoplankton: *Prochlorococcus* sp., *Synechococcus* sp. and small eukaryotes; four of them share the characteristics of the former nanophytoplankton: two green algae groups (Chlorophyceae and Eugleno-Prasinophyceae) and two Haptophyta groups (non-calcifying and calcifying or coccolithophores); and diatoms and dinoflagellates share the same physiological characteristics of the former dinoflagellates and hence constitute together the microphytoplankton size class. The optical properties ($a^*_{PH}(\lambda)$, $a^*_{PS}(\lambda)$, $b^*_{PH}(\lambda)$ and br_{PH}) for the PFTs in the picoplankton size class were the average of the respective spectra for $P^{(3)}$, $P^{(6)}$ and $P^{(9)}$; the spectrum for the PFTs in the nanoplankton size class was the average for $P^{(2)}$, $P^{(5)}$, $P^{(7)}$ and $P^{(8)}$; and the spectrum for the PFTs in the microplankton size class was the average for $P^{(1)}$ and $P^{(4)}$.

Given that PFTs in the same size class share common physiological traits and are consumed by predators with the same preference, this reference configuration of BFM recreates a situation where the PFTs in a given PSC are ecologically equivalent, as they use resources identically and are eaten by the same predators. The assumption of the reference configuration is relaxed in the list of experiments when PFT differentiations are introduced (Section 2.2.3). When deviating from this reference configuration by including physiological differences among PFTs, the observable result of competition, that is, the number of prey types in the same PSC that can coexist under given environmental conditions, depends on the grazing formulation. Adopting the standard BFM description, PFT mortality due to zooplankton grazing is larger for the most abundant ones, so predation will influence, but not limit, the number of coexisting PFTs. The grazing formulation was adjusted to limit the number of prey species that can coexist under given environmental conditions within each PSC. Therefore, the BFM recreates a situation where the PFTs in a given PSC face stronger competition, as they use resources differently but are eaten by the same predators with identical preference, which limits to just one the number of coexisting PFTs.

The full list of BFM equations can be found elsewhere (Vichi et al., 2015). The next subsections report those equations connected to optical and biogeochemical coupling, namely, the growth of PFTs, photosynthesis and photoacclimation, the production of CDOM and NAP and the details about the modifications incorporated in the grazing formulation.

2.2.2.1. Phytoplankton growth. Every PFT in the model is composed of several common constituents, and only carbon (P_C) and chlorophyll (P_{Chl}) are related to optical-biogeochemical coupling. Their dynamic equations are composed of source and loss terms, which include photosynthesis, respiration, exudation, biochemical synthesis and grazing. The nine PFTs share the same form of primitive equations but are differentiated in terms of the values of the physiological parameters that depend on the phytoplankton size class they are subdivided from (Lazzari et al., 2012; Vichi et al., 2015), and the values are listed in Table B1 of Appendix B.

Carbon

The change in carbon content for each PFT is the result of the specific growth rate minus the specific loss terms of respiration and exudation (all in d^{-1}) and the losses due to predation (mg C m^{-3} d^{-1}):

$$dP^{(i)}_C/dt = \left(photosynthesis^{(i)}_P - respiration^{(i)}_P - exudation^{(i)}_P\right) \times P^{(i)}_C - grazing^{(i)}_Z;\ i = 1\ \text{to}\ 9$$

The specific growth rate of each phytoplankton species (*photosynthesis*$_P$, d^{-1}) is computed as the maximal productivity rate ($r0_P$ d^{-1}) regulated by temperature (et_P, dimensionless), nutrients (fg_P, dimensionless) and light through an increasing, saturating function of the number of photons it has absorbed. Such a function is known as the photosynthesis-irradiance (PI) curve, and the BFM uses the exponential representation presented in Webb et al. (1974). The initial slope of the curve is the product of the average chlorophyll-specific absorption cross-section ($\overline{a^*_{PS}}$, m^2 $mgChla^{-1}$), the photochemical efficiency or quantum yield (ϕ, mgC μE^{-1}) and the P_{Chl} to P_C quotum (θ, mgChl mgC^{-1}), and hence accounts for how much light is absorbed by phytoplankton cells and with which efficiency this light is used to fix carbon.

$$photosynthesis_P^{(i)} = r0_P^{(i)} \times et_P^{(i)} \times fg_P^{(i)} \times \left(1 - \exp\left(\frac{-\phi^{(i)} \times \overline{a_{PS}^{*(i)}} \times \theta^{(i)} \times PAR}{r0_P^{(i)}}\right)\right) \quad (15)$$

When the spectral composition of light is considered, the number of absorbed photons available for photosynthesis by a PFT at a given depth depends on its photosynthetic action spectrum ($a_{PS}^{*}(\lambda)$, Fig. 1**d**) and on the light spectrum at this depth,$E_0(\lambda)$. Total absorbed irradiance is the integral of $a_{PS}^{*}(\lambda)$ times $E_0(\lambda)$ between 387.5 and 800 nm (μmol quanta mg Chla^{-1} d^{-1}). For an equal PAR and an equal $\overline{a_{PS}^{*}}$, the total absorbed irradiance is higher when the spectral shapes of $a_{PS}^{*}(\lambda)$ and $E_0(\lambda)$ are more similar.

$$photosynthesis_P^{(i)} = r0_P^{(i)} \times et_P^{(i)} \times fg_P^{(i)} \times \left(1 - \exp\left(\frac{-\phi^{(i)} \times \theta^{(i)} \times \int_{387.5}^{800} a_{PS}^{*(i)}(\lambda) \times E_0(\lambda) d\lambda}{r0_P^{(i)}}\right)\right) \quad (16)$$

In both cases, the value for ϕ was set to 4.8e-4 mgC μmol quanta^{-1} for all PFTs; hence, the larger the total absorbed irradiance was, the higher the photosynthetic rate under sub-saturating light was.

Chlorophyll

The chlorophyll equation is composed of a term for net chlorophyll synthesis (mg Chl m^{-3} d^{-1}) and a term representing the losses due to grazing:

$$dP_{Chl}^{(i)}/dt = net\ synthesis_P^{(i)} - \left(grazing_Z^{(i)} \times \theta^{(i)}\right);\ \mathrm{i} = 1 \text{ to } 9$$

Net chlorophyll synthesis (*net synthesis*$_P$) includes the process of photoacclimation in the content of photosynthetic pigments, nutrient availability and a turnover rate. The acclimation part is taken from Geider et al. (1997) and regulates the amount of chlorophyll in the cell (ρChl) according to the nondimensional ratio between the realized photosynthetic rate and the maximum potential photosynthesis, multiplied by the maximum P_{Chl} to P_C ratio (θmax_P). The denominator in ρChl now considers the spectral composition of $E_0(\lambda)$ and the action spectrum $a_{PS}^{*}(\lambda)$, the same as photosynthesis did before (Eq. (16)). The combined nutrient regulating factor (fnp_P, dimensionless) implies that Chl synthesis is reduced in regions limited by P, such as the Mediterranean Sea (Lazzari et al. 2012). The losses are represented by a nutrient-regulated turnover rate ($dChl_P$, d^{-1}) and a relaxation term to θmax_P.

$$netproduction_P^{(i)} = \left(photosynthesis_P^{(i)} - respiration_P^{(i)} - exudation_P^{(i)}\right) \times P_C^{(i)} \quad (18)$$

$$\rho Chl^{(i)} = \theta max_P^{(i)} \times \frac{photosynthesis_P^{(i)}}{\phi^{(i)} \times \theta^{(i)} \times et_P^{(i)} \times \int_{387.5}^{800} a_{PS}^{*(i)}(\lambda) \times E_0(\lambda) d\lambda} \quad (19)$$

$$netsynthesis_P^{(i)} = \begin{array}{c} fnp_P^{(i)} \times \rho Chl^{(i)} \times netproduction_P^{(i)} \\ -dChl_P^{(i)} \times \left(1 - fnp_P^{(i)}\right) \times P_{Chl}^{(i)} - netproduction_P^{(i)} \times \left(P_{Chl}^{(i)} - \theta max_P^{(i)} \times P_C^{(i)}\right) \end{array} \quad (20)$$

The formulations for the temperature (et_P) and nutrient regulations (fg_P and fnp_P) and for respiration and exudation are detailed in Appendix B.

2.2.2.2. CDOM and non-algal particles. **CDOM**

CDOM is produced by some of the processes that produce dissolved organic carbon (DOM), namely, the exudation of phytoplankton and the mortality of phytoplankton and bacteria (both in mgC m^{-3} d^{-1}). Hence, labile CDOM ($R_l^{(1)}$) is explicitly resolved as a 2% fraction (f_{CDOM}) of the labile pool of DOM excreted by nano- and microzooplankton ($R_C^{(1)}$), and semi-labile CDOM ($R_l^{(2)}$) is resolved as a 2% fraction of the semi-labile pool of DOM exuded by phytoplankton ($R_C^{(2)}$). Similar to DOM, both CDOM types are consumed by bacteria, but unlike DOM, they are photobleached at a rate that is maximized (l_{CDOM}, d^{-1}) when the PAR is above I_{CDOM} (μmol quanta m^{-2} d^{-1}) and decreases linearly at lower PAR values (Table 2). The formulations for zooplankton excretion, phytoplankton exudation and bacterial uptake rates are detailed in Appendix B. Semi-refractory CDOM ($R_l^{(3)}$) is also included, but in our setup, this type is not produced by any living component and is only photobleached and remineralized at a very slow temperature-regulated (et_C) rate (d_{CDOM}, d^{-1}), which in practice means that this pool is negligible in the illuminated part of the water column and remains close to the initialization values for the rest, with the objective of representing the vertical distribution of CDOM absorption observed in the deep Mediterranean Sea (Catalá et al., 2018).

$$dR_l^{(1)}/dt = \left(\sum_{j=5}^{6} excretion_Z^{(j)} \times \left(1 - \varepsilon c_z^{(j)}\right)\right) \times f_{CDOM} - uptakeR1l - l_{CDOM} \times \min(PAR/I_{CDOM}, 1) \times R_l^{(1)} \quad (21)$$

$$dR_l^{(2)}/dt = \left(\sum_{i=1}^{9} activityexudation_P^{(i)} \times P_C^{(i)}\right) \times f_{CDOM} - uptakeR2l - l_{CDOM} \times \min(PAR/I_{CDOM}, 1) \times R_l^{(2)} \quad (22)$$

$$dR_l^{(3)}/dt = \left(-l_{CDOM} \times \min(PAR/I_{CDOM}, 1) - (et_C \times d_{CDOM})\right) \times R_l^{(3)} \quad (23)$$

NAP

The carbon fraction of non-algal particles ($R_C^{(6)}$) is produced by zooplankton by egestion/excretion (mgC m^{-3} d^{-1}). All excretions by mesozooplankton are assumed to be particulate. In nano- and microzooplankton, a constant 60% (εc_Z) of the released carbon is considered particulate. $R_C^{(6)}$ is consumed by bacteria. The formulations for excretion and consumption rates are detailed in Appendix B.

$$dR_C^{(6)}/dt = \left(\sum_{j=3}^{6} excretion_Z^{(j)} \times \varepsilon c_z^{(j)}\right) - uptakeR6c \quad (24)$$

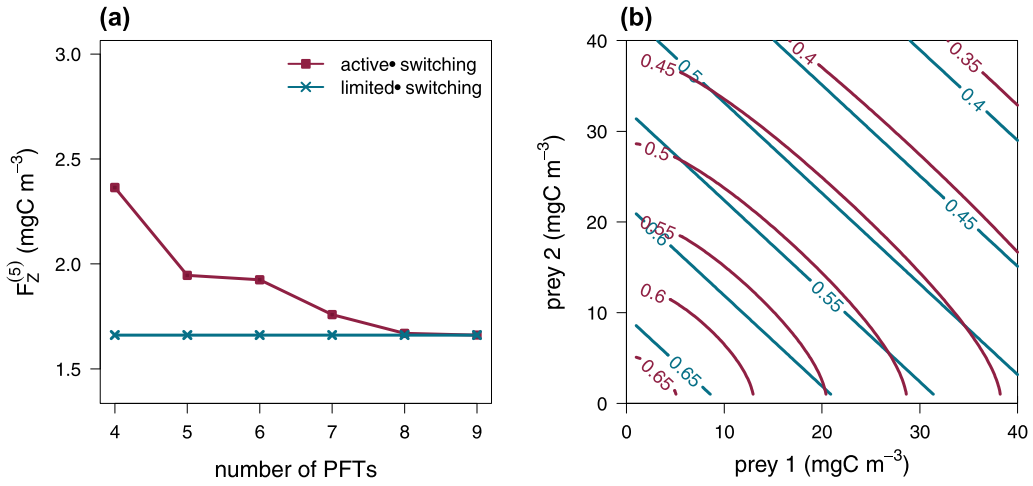

Fig. 3. Behaviour of two grazing formulations, active-switching and limited-switching functional response: **(a)** total amount of food available to microzooplankton ($F_Z^{(5)}$) as a function of the number of PFTs, and **(b)** isoclines of total ingestion of microzooplankton ($I_Z^{(5)}$) as a function of the biomass of two prey of the same size class.

There is an additional source of non-algal particles as a result of zooplankton and bacteria adjusting their internal quota to their optimal values that we have not detailed here but whose details can be found in Vichi et al. (2015, 2007).

2.2.2.3. Grazing. Phytoplankton are grazed by four types of predators: nanoheterotrophs ($Z^{(6)}$), microzooplankton ($Z^{(5)}$), omnivorous mesozooplankton ($Z^{(4)}$) and carnivorous mesozooplankton ($Z^{(3)}$). The multiple-prey functional response describes the way the ingestion rate of zooplankton type j ($I_Z^{(j)}$, mgC m^{-3} d^{-1}) varies with the biomass of the predator ($Z_C^{(j)}$, mgC m^{-3}) and the total prey density available to that predator ($F_Z^{(j)}$, mgC m^{-3}). In the BFM, it is described by a Michaelis-Menten function, as follows:

$$I_Z^{(j)} = gmax_Z^{(j)} \times et_Z^{(j)} \times \frac{F_Z^{(j)}}{F_Z^{(j)} + h_Z^{(j)}} \times Z_C^{(j)}; \mathrm{j} = 3 \text{ to } 6$$

where $gmax_Z$ is the maximum uptake capacity (d^{-1}), et_Z is the metabolic temperature response (dimensionless), and h_Z is a predation efficiency constant limiting the chances of encountering prey (Table B2 in Appendix B). The formulation for the temperature regulation (et_Z) is detailed in Appendix B.

The total amount of food available to a given predator is computed considering the biomasses of all possible prey among bacteria, phytoplankton and zooplankton ($X \in \{B^{(1)}, P^{(1-9)}, Z^{(3-6)}\}$, mgC m^{-3}), weighted by the relative preference of the predator for each prey type.

$$F_Z^{(j)} = \sum_{i=1}^{14} p_j^{(i)} \times X_C^{(i)} \tag{26}$$

For each prey, the grazing rate by all its predators ($grazing_P$, mg C m^{-3} d^{-1}) can be expressed as the sum of the total ingestion of each predator $I_Z^{(j)}$, weighted by the relative preferences of the predator for that particular prey type and normalized by the relative proportion of the biomass of that prey in the total food available.

$$grazing_Z^{(i)} = \sum_{j=3}^{6} I_Z^{(j)} \times p_j^{(i)} \times \frac{X_C^{(i)}}{F_Z^{(j)}} \tag{27}$$

The preference $p_j^{(i)}$ represents the dimensionless weight of each prey i in the predator j diet, which corresponds to the relative proportion that this prey occurs in the diet of this predator vs. the relative proportion of this prey type in the environment (Gentleman et al., 2003). There are many definitions of preferences in the literature. Multiple prey functional responses are classified according to whether these preferences are constant or density-dependent (i.e., no-switching vs. switching) and whether these preferences are derived from inherent differences among prey (i.e., passive selection) vs. active behavioural changes by the predator (i.e., active selection) (Gentleman et al., 2003).

Active-switching grazing formulation

Preference formulation in the BFM is described according to Baretta-Bekker et al. (1998) and includes density-dependent preferences (switching) and a mathematical characterization of active behavioural changes (active) (Eq. 38 in Vichi et al. 2007). Hence, the preference of a grazer for a given prey combines two elements, the availability of prey i to predator j ($\delta_j^{(i)}$), which is constant, encapsulates the size constraints of the predator–prey relationship and is set in a diet matrix (Table B2), and the capture efficiency of prey i by predator j.

$$p_j^{(i)} = \delta_j^{(i)} \frac{X_C^{(i)}}{X_C^{(i)} + f_{min}^{(j)}} \tag{28}$$

Capture efficiency is a density-dependent term in a Michaelis-Menten form and hence characterizes how predators may preferentially select the most abundant prey, reflecting an increase in efficiency at capturing or handling a given prey type as its biomass increases relative to the others. The purpose of this formulation is to include subscale effects of pooling prey in the relatively large volume represented by a model grid cell. Preys of different types can be assumed to be distributed in separate patches, and individual prey patches below a certain size are less likely to be grazed upon compared to the larger patches, which is expressed by the f_{min} parameter (Butenschön et al., 2016). To ensure that the total prey biomass available to a given predator ($F_Z^{(j)}$) does not vary as total prey biomass is subdivided into more prey types and to keep predation consistent, the value of f_{min} needs to be adjusted (further details are in Appendix C).

Limited-switching grazing formulation

The total prey biomass available to a given predator remains constant independent of the number of PFTs subdivided within a given PSC if the capture efficiency is a function of the PSC biomass itself. We modified Eq. (28) to make the capture efficiency of a given PFT not dependent on the biomass of the PFT (X_i) but rather on the total biomass of the PSC from which the PFT was subdivided (Table 1):

$$p_j^{(i)} = \delta_j^{(i)} \frac{PSC_C^{(i)}}{PSC_C^{(i)} + f_{min}^{(j)}} \tag{29}$$

where for picophytoplankton: $PSC_C^{(3,6,9)} = P_C^{(3)} + P_C^{(6)} + P_C^{(9)}$; for nano-

Table 3
Characteristics of the model experiments performed in terms of their differences from the reference configuration (EXP-C).

	EXP-C	EXP-0	EXP-1	EXP-2	EXP-3
Number of optically different phytoplankton groups	3	9	9	9	9
Absorption cross-sections considered	$\overline{a^*_{PS}}$	$\overline{a^*_{PS}}$	$a^*_{PS}(\lambda)$	$a^*_{PS}(\lambda)$	$a^*_{PS}(\lambda)$
Maximal productivity of $P^{(1)}$ ($r0_P^{(1)}$)	1.5	1.5	1.5	2.5	2.5
Excreted fraction of primary production of $P^{(1)}$ ($\beta_P^{(1)}$)	0.15	0.15	0.15	0.05	0.05
Maximum sinking velocity for $P^{(1)}$ ($\omega sink^{(1)}$)	2.5	2.5	2.5	5.0	5.0
Nutrient stress threshold for sinking of $P^{(1)}$ ($lsink^{(1)}$)	0.75	0.75	0.75	0.7	0.7
Silica limitation for $P^{(1)}$	no	no	no	yes (internal)	yes (internal)
Minimum quotum Si:C for $P^{(1)}$ ($Qmin_{Si}^{(1)}$)	0	0	0	0.007	0.007
Reference quotum Si:C for $P^{(1)}$ ($Qopt_{Si}^{(1)}$)	0	0	0	0.01	0.01
Availability of $P^{(1)}$ ($\delta_P^{(1)}$) to $Z^{(5)}$	0.1	0.1	0.1	0.7	0.7
Availability of $P^{(1)}$ ($\delta_P^{(1)}$) to $Z^{(3)}$	1.0	1.0	1.0	0	0
Reference PIC:POC ratio of $P^{(5)}$ ($PIC:POC^{(5)}$)	0.3	0.3	0.3	1	1
Quantum yield of $P^{(1)}$ ($\phi^{(1)}$)	4.8e-4	4.8e-4	4.8e-4	4.8e-4	1.5e-3

phytoplankton: $PSC_C^{(2,5,7,8)} = P_C^{(2)} + P_C^{(5)} + P_C^{(7)} + P_C^{(8)}$; and for microphytoplankton: $PSC_C^{(1,4)} = P_C^{(1)} + P_C^{(4)}$. With this change, within a given PSC, all prey would become perfectly substitutable from the point of view of the predator. Given that their constant availabilities ($\delta_j^{(i)}$) are equal, they would experience the same grazing pressure ($grazing_P$). A way to visualize this behaviour is by noting that the size of the prey patch that the predator can detect and eat now applies to the total food in a PSC instead of to each individual prey. Since this is not a complete no-switching formulation because the no-switching behaviour occurs only within the PSC, we call it limited-switching.

Outcome of apparent competition

The relative fitness of different PFTs is determined by their photosynthetic growth rate and hence by the efficiency with which they use resources and by their mortality rate (e.g., two PFTs compete for a common pool of resources, and they interact via the apparent competition that occurs through the shared common predator). Hence, the outcome of competition depends on the grazing formulation. With the limited-switching formulation, $F_Z^{(j)}$ was constant, independent of how many PFTs there were in a particular size class (Fig. 3**a**, blue). With the active-switching formulation, $F_Z^{(j)}$ decreased as the phytoplankton compartment was subdivided into more PFTs (Fig. 3**a**, red). With the adjustment in the value of the parameter $f_{min}^{(i)}$ (further details in Appendix C), both grazing formulations were comparable in terms of $F_Z^{(j)}$ with a phytoplankton compartment represented by 9 PFTs. Therefore, both grazing formulations were comparable in terms of $F_Z^{(j)}$, which means that grazers obtained the same amount of food but the prey they preferentially chose was different between the two formulations, which is illustrated by the different $I_Z^{(j)}$ isoclines (Fig. 3**b**, blue vs. red curves).

With the original BFM active-switching formulation, the constant-ingestion line of one predator considering two prey types of the same size class was nonlinear (Fig. 3**b**, blue), which indicates that when the density of prey 2 decreases, the predator feeds comparatively more on prey 1 (Holt, 1983). PFTs with a competitive advantage that permits them to have higher growth rates were grazed comparatively more than other PFTs with lower growth rates. This creates predation refuges for low-density prey (Gentleman et al., 2003; Holt, 1983) that permit them to escape predation; thus, all PFTs tended to coexist. With the limited-switching formulation, on the other hand, all PFTs within a given size class shared the same grazing pressure independently of how they were labelled. The constant-ingestion line considering two prey types of the same size class was linear (Fig. 3**b**, red), which indicated that both preys were always in the diet of the predator and were completely interchangeable (Holt, 1983). PFTs with a competitive advantage that permits them to have higher growth rates were grazed equally to other PFTs in their same size class; thus, the former dominated the community, and the latter were eventually excluded.

2.2.3. Model simulations

Three-dimensional (3D) simulations were used to investigate the interaction of optically different PFTs with the underwater spectral light field in a complex real system. In the 3D configuration for the Mediterranean Sea, the BFM was coupled with the OGSTM transport model. Details of the OGSTM and its coupling with the BFM can be found elsewhere (Lazzari et al., 2010, Salon et al., 2019). The horizontal resolution was 1/16th of degree with 70 layers in the vertical from 0 to 4848 m, ranging from 3 m deep at the surface and gradually increasing in thickness with depth thereafter, reaching 10 m at 100 m and 20 m at 250 m. State variables initialization, physical forcing, riverine runoff and boundary conditions at the Strait of Gibraltar were those reported in Lazzari et al. (2016, 2012). The only difference was that the 3D initialization fields for the elemental components of phytoplankton (C, N, P, Si and Chl) were set to keep the total biomass equal to the original 4 phytoplankton groups used in previous applications of the BFM in the Mediterranean Sea (Lazzari et al., 2012). The simulations run from 2011 to 2015, saving output on a monthly basis, and we presented results for 2015.

To explore how the inclusion of optical and functional differences among PFTs affects their distribution, we performed a sequence of experiments including PFT differentiations with respect to the reference configuration (section 2.2.2). Each experiment consisted of two runs, one using the active-switching formulation and the other using the limited-switching grazing formulation. Specific parameter values of the experiments are summarized in Table 3**,** and the list includes the following:

- **EXP-C**: a reference experiment that used the reference 9 PFT configuration as described in section 2.2.2 (i.e., functional and optical properties, and trophic interactions of PFTs within a given size class were identical).
- **EXP-0:** included non-spectral optical differences among all the PFTs. Each of the 9 PFTs uses its own average chlorophyll-specific absorption cross-section ($\overline{a^*_{PS}}$). Photosynthesis was computed as described in Eq. (15), and $\overline{a^*_{PS}}$ values are those indicated in the insert in Fig. 1**d**.
- **EXP-1:** included spectral optical differences among all the PFTs. Each of the 9 PFTs used its own light action spectra ($a^*_{PS}(\lambda)$). Photosynthesis was computed as described in Eq. (16), and $a^*_{PS}(\lambda)$ values are those represented in Fig. 1**d.**
- **EXP-2:** included some functional differentiation among PFTs in the same PSC. Within microphytoplankton, diatoms ($P^{(1)}$) obtained their parameter values used in previous applications of the BFM, which means that relative to dinoflagellates ($P^{(4)}$), they are limited by silica, have higher productivity rates, excrete a smaller fraction of primary production, sink faster and are grazed upon more by microzooplankton ($Z^{(5)}$) than by carnivorous zooplankton ($Z^{(3)}$). Within

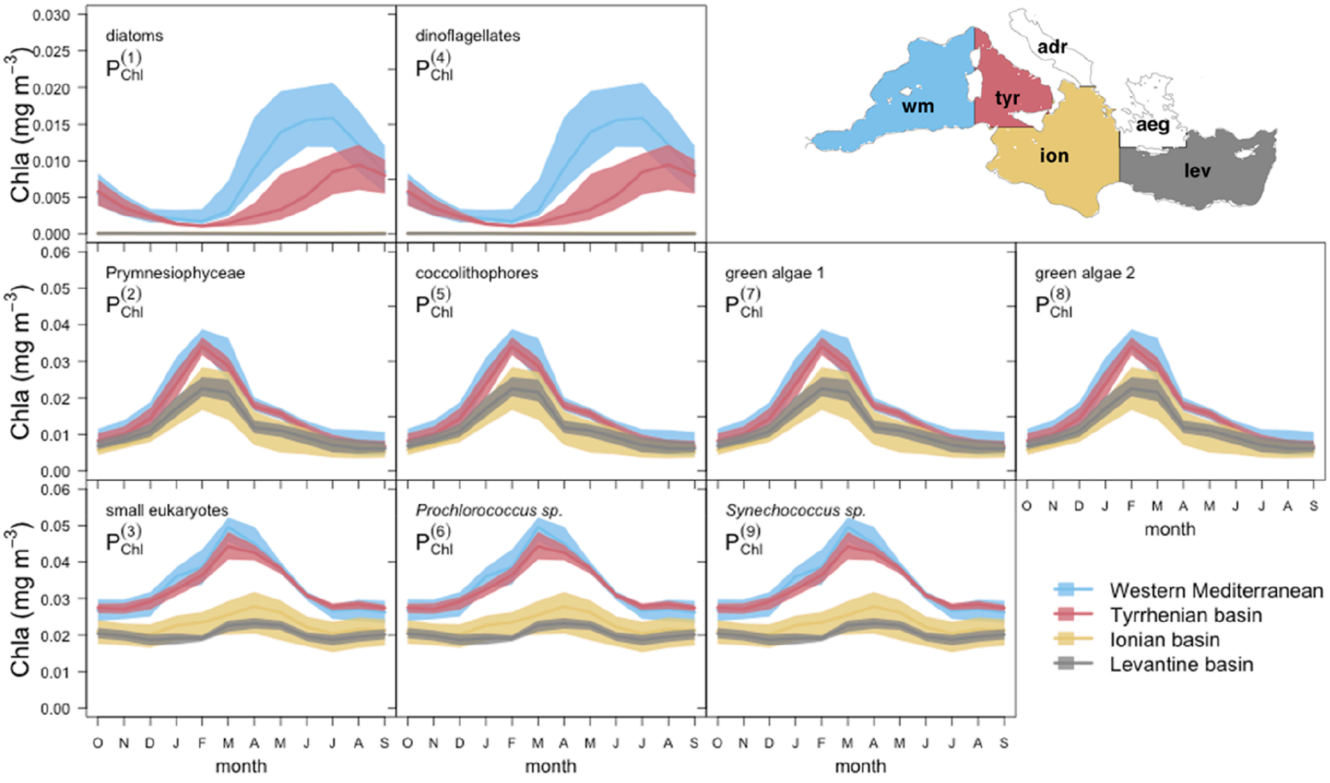

Fig. 4. EXP-C results: seasonal evolution of the median chlorophyll concentration ($P_{Chl}^{(i)}$) in the z_{eu} of the 9 PFTs in four major areas of the Mediterranean Sea. Coloured areas show the interquartile range of values for the basin. Only EXP-C with active-switching is shown, as the results for EXP-C with limited-switching are identical.

nanophytoplankton, the PIC:POC production ratio changed to 1 for coccolithophores and 0 for the rest (Krumhardt et al., 2017).

- **EXP-3:** equal to EXP-2, but it increased the quantum yield (ϕ) of diatoms ($P^{(1)}$) to 1.5e-3 mgC μmol quanta^{-1}, so the product of their $\overline{a_{PS}^{*}}$ times ϕ equals the value used in previous applications of the BFM in the Mediterranean Sea (Lazzari et al., 2012).

Both types of grazing formulations, active-switching (EXP-*n* active-switching) and limited-switching grazing formulation (EXP-*n* limited-switching), were tested for each experiment.

2.3. Observations

Model output was compared against a comprehensive set of observational data of PFT concentrations, both from field sampling and from satellite products.

2.3.1. Compilation of HPLC pigments

Pigment data were obtained from published HPLC datasets that contained observations in the Mediterranean Sea: the MAREDAT dataset (Peloquin et al., 2013) available in PANGAEA, as well as the TARA expedition (Boss and Claustre, 2014, 2012), Boum08 cruise (Behrenfeld and Dall'Olmo, 2020) and Boussole monitoring site (Antoine, 2012) datasets, which are all available in SeaBASS. These datasets were quality controlled following (Aiken et al., 2009). In all the datasets, TChla (mg m^{-3}) encompassed all the reported Chla derivatives, monovinyl Chla, divinyl Chla and chlorophyllide a. Total accessory pigment concentration (AP, mg m^{-3}) was calculated as the summed concentration of all carotenoids and chlorophyll *b* and c. Total pigment concentration (TP, mg m^{-3}) was calculated as the summed concentration of AP and TChla. Samples were excluded if i) TChla was zero or less and ii) the difference in TChla and AP was more than 30% of the TP. Complete cruises were excluded if i) the regression between TChla and AP for the entire cruise had a slope outside the range of 0.7–1.4 or explained less than 90% of the total variance and ii) less than 85% of the samples of that particular cruise passed the previous criteria.

2.3.2. Determination of PFTs in situ from diagnostic pigments

For the taxonomic identification of PFTs, we employed the diagnostic pigments (DP) method, which is based on the use of pigments as markers for the main algal groups (Vidussi et al., 2001). This method considers only the pigments that are more closely linked to a single PFT, and for these pigments, their occurrence in other groups is neglected (Uitz et al., 2006). We used the Mediterranean-specific algorithms proposed by DiCicco et al. (2017) that use seven DPs to compute the fraction of diatoms (DIATO), dinoflagellates (DINO), haptophytes (HAPTO), Cryptophyceae (CRYPTO), prokaryotes (PROKAR) and Chl b-containing algae (GREEN) relative to TChla. For the in situ HPLC compilation, we limited the analysis to the samples that contained the measurement of the seven DPs, which reduced our PFT Chla concentration dataset to 8199 samples, i.e., 94% of the initial HPLC quality-controlled data.

2.3.3. CMEMS satellite product

The regional DP algorithm for the Mediterranean Sea was also used to derive the Chl concentrations of the same six PFTs from remotely sensed TChla. The method follows a global approach (Hirata et al., 2011) based on the existing covariability between the in situ chlorophyll fraction of PFTs and the corresponding TChla concentration (Chisholm, 1992; Hirata et al., 2011; Uitz et al., 2006). The empirical relationships between in situ TChla and the fraction of each PFT, which was estimated with the DP method described above, were used to estimate the contribution of each PFT to the Mediterranean Sea assemblage in terms of chlorophyll concentration. The final in situ PFT estimation formulas and the regional satellite algorithms, with their references, are fully described in DiCicco et al. (2017).

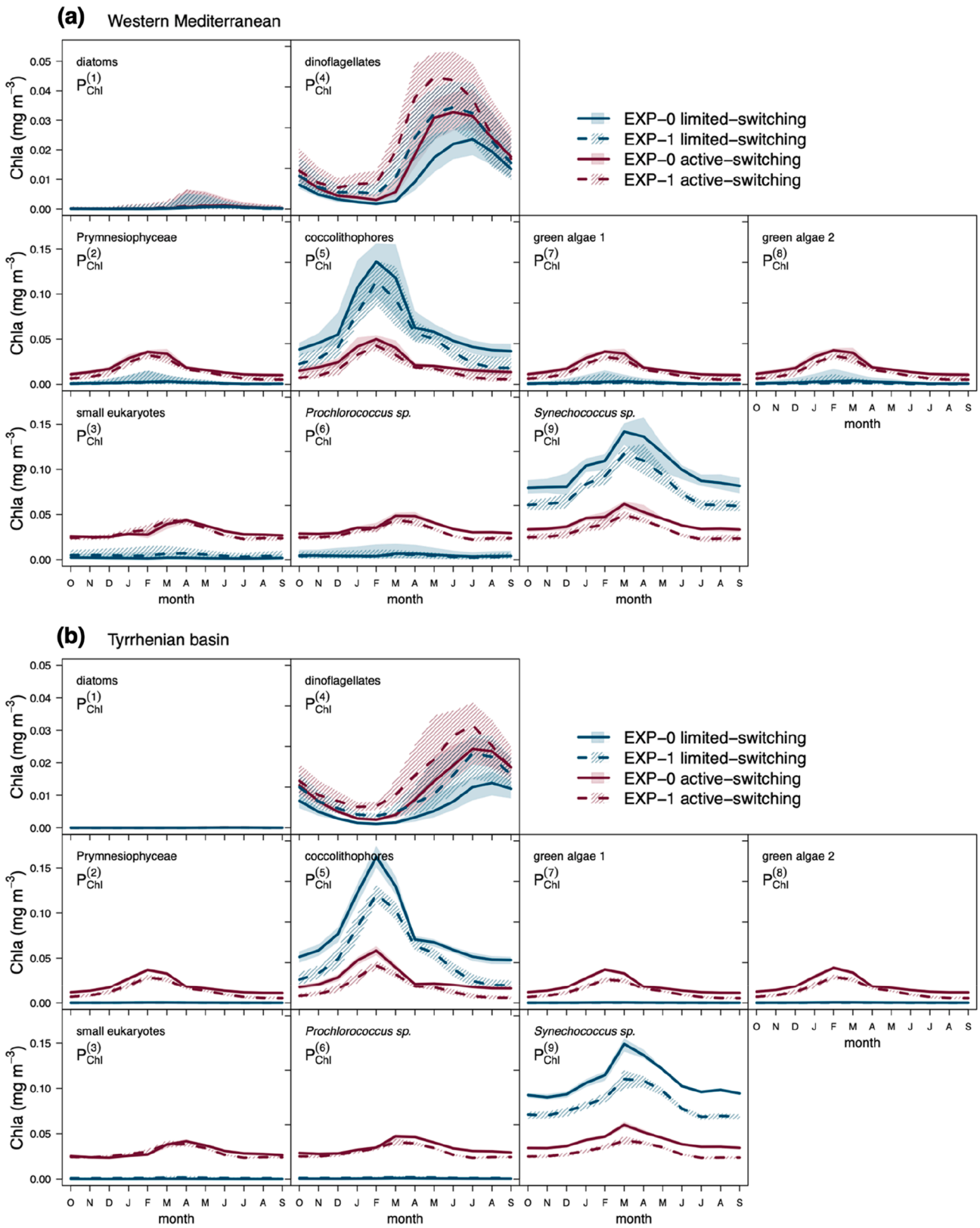

Fig. 5. EXP-0 and EXP-1 results: seasonal cycle of the median chlorophyll concentration ($P_{Chl}^{(i)}$) in the z_{eu} of the 9 PFTs in the **(a)** western Mediterranean basin and **(b)** Tyrrhenian basin. Solid lines indicate results from EXP-0, and dashed lines indicate results from EXP-1. In red, the respective experiment runs with an active-switching formulation, and in blue, the respective experiment runs with a limited-switching grazing formulation. Coloured areas show the interquartile range of Chl values in the basin for each month.

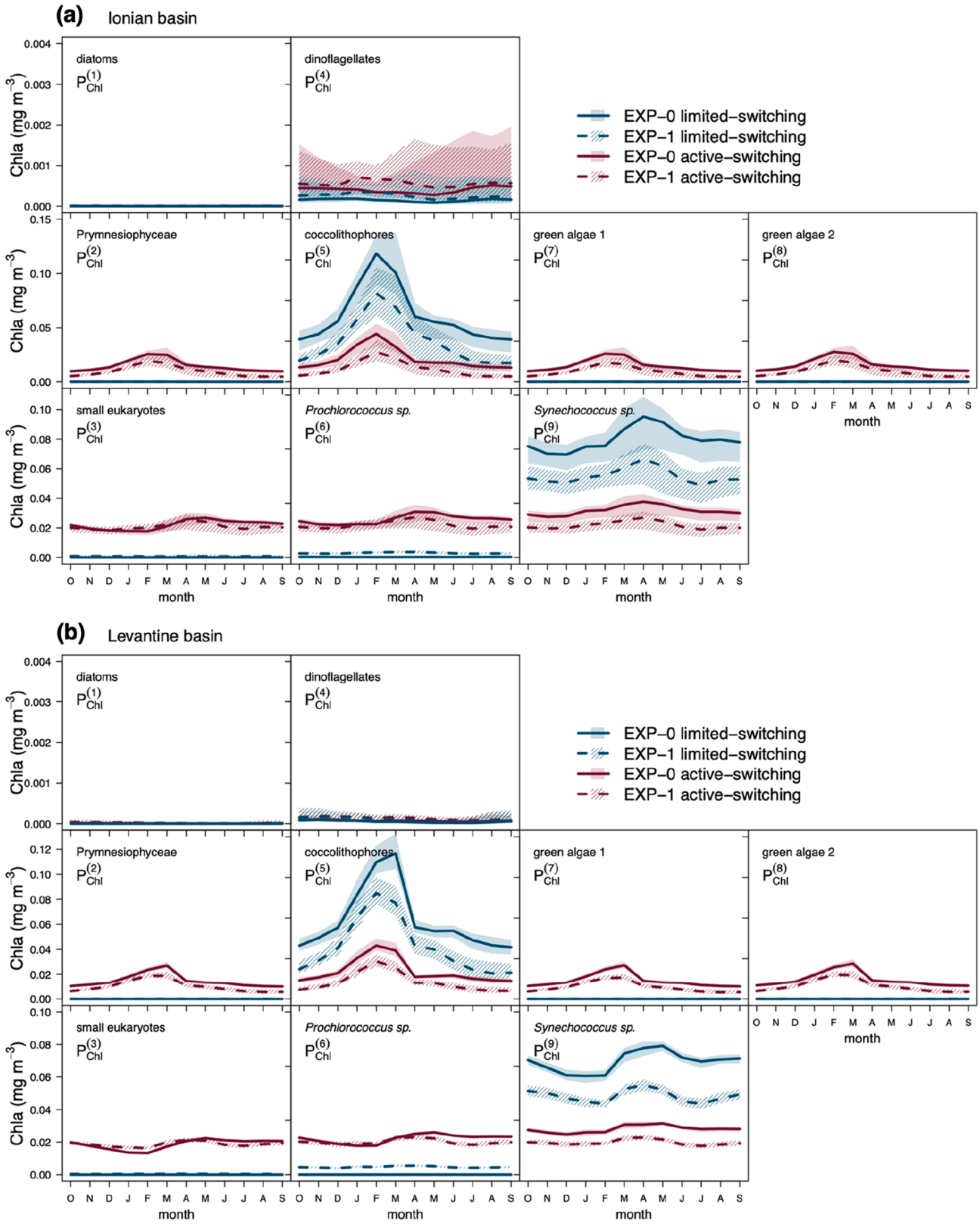

Fig. 6. The same as Fig. 5 for the **(a)** Ionian and **(b)** Levantine basins.

The PFT algorithms were applied to the L4 chlorophyll *a* product of 2015 available from the Copernicus Marine Environment Monitoring Service (CMEMS). The CMEMS chlorophyll product (E.U. Copernicus Marine Service Information, 2020) features optical properties of inshore (AD4 algorithm, D'Alimonte and Zibordi (2003)) and offshore (MedOC4 algorithm, Volpe et al. (2007)) waters, and it was released as a merged Case I–Case II product (D'Alimonte et al., 2003; Volpe et al., 2019).

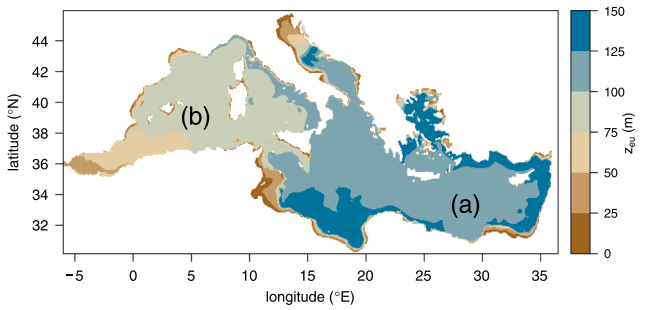

Fig. 7. Annual mean of the depth of the euphotic zone (z_{eu}) computed as the depth where the PAR reaches 1% of the PAR at the surface. (a) and (b) indicate the positions of the two example locations used in Fig. 8.

3. Results

3.1. Reference experiment: Same physiology and shared predation

Results of EXP-C (i.e., PFTs within each PSC were clones) showed how the phytoplankton community composition and distribution in EXP-C with active-switching were equivalent to those in EXP-C with limited-switching. The seasonal evolution of the median chlorophyll concentration in the euphotic zone (z_{eu}) of all PFTs in EXP-C with active-switching is shown in Fig. 4. Given that the three picophytoplankton PFTs, the four nanophytoplankton PFTs and the two microphytoplankton PFTs were functionally and optically identical, the two grazing formulations produced the same result, and the chlorophyll in each size class was divided homogeneously among the PFTs that integrated the size class. The only difference was how they were labelled. Note that whereas pico- and nanoplanktonic PFTs were present in the four basins (second and third rows in Fig. 4, respectively), the presence of microplanktonic PFTs in the easternmost basins was negligible (first row in Fig. 4).

The same behaviour of EXP-C with the two grazing formulations and the even partition of chlorophyll among PFTs in the same PSC is because PFTs in the same PSC use resources identically and are eaten by the same predators (i.e., they are clones). In the following, we used this virtual environment to start including physiological differences among PFTs. From EXP-0 to EXP-3, we sequentially differentiated traits regarding absorption cross-sections, without (EXP-0) and with spectral differentiation (EXP-1), and functional characteristics (EXP-2 and EXP-3); we tested them both with active and limited-switching formulations. Before presenting the results, it is worth noting that whereas the active-switching formulation tends to hide the effect of the physiological differences by the biomass homogenization promoted by grazing, the limited-switching formulation permits to depict situations where PFTs in a given size class face a stronger possible competition. This latter formulation allows us to see the effect of a physiological difference in giving place to the dominance of a given PFT under given environmental conditions.

3.2. Competitive advantage: Differences in optical properties (spectral vs. Non spectral)

The result of competition among PFTs depended on which characteristic differentiated PFTs within each size class. In EXP-0, the competitive advantage was simply a higher $\overline{a^*_{PS}}$ that allowed the absorption of more light under any light regime. In EXP-1, the competitive advantage was provided by a $a^*_{PS}(\lambda)$ that, under a given $E_0(\lambda)$, allowed the PFT to absorb more light and to have higher growth rates. The PFT with a better match of its absorption coefficients to the incoming spectral $E_0(\lambda)$ would have a competitive advantage with respect to the others. In both cases, (i.e., non-spectral in EXP-0 and spectral in EXP-1), the success or coexistence of the PFTs that had a competitive advantage with the others depended on the grazing formulation that maximized competition (limited-switching) or promoted coexistence (active-switching).

3.2.1. Results under promoted coexistence: active-switching

The active-switching formulation promoted the coexistence of PFTs, minimizing the competitive advantage that higher absorption coefficients represented, independently if they were averaged or spectrally resolved. PFTs whose $\overline{a^*_{PS}}$ permitted them to absorb more light and have higher growth rates were grazed comparatively more than other PFTs with lower growth rates. Within pico- and nanoplankton, although the PFTs within a particular size class did not share exactly equal amounts of chlorophyll, as when they were identical in EXP-C, they were close to this allocation (Figs. 5 and 6, red lines). In contrast, in microphytoplankton, dinoflagellates ($P^{(4)}$) were more concentrated than diatoms ($P^{(1)}$) throughout the year in all basins, although the latter were not completely excluded. In any case, this formulation tended to maximize the variability of optical properties found in the phytoplankton community, but it was limited when trying to see which was the best competitor.

3.2.2. Results under maximal competition: limited-switching

The limited-switching formulation, however, maximized competition; that is, under constant environmental conditions, the group that retained the competitive advantage succeeded, and the rest were grazed until extinction. In EXP-0, the PFTs whose $\overline{a^*_{PS}}$ permitted them to absorb more light and have higher growth rates were grazed equally as other PFTs, and the latter were eventually eliminated. This led to the dominance of *Synechococcus* sp. ($P^{(9)}$) within picophytoplankton,

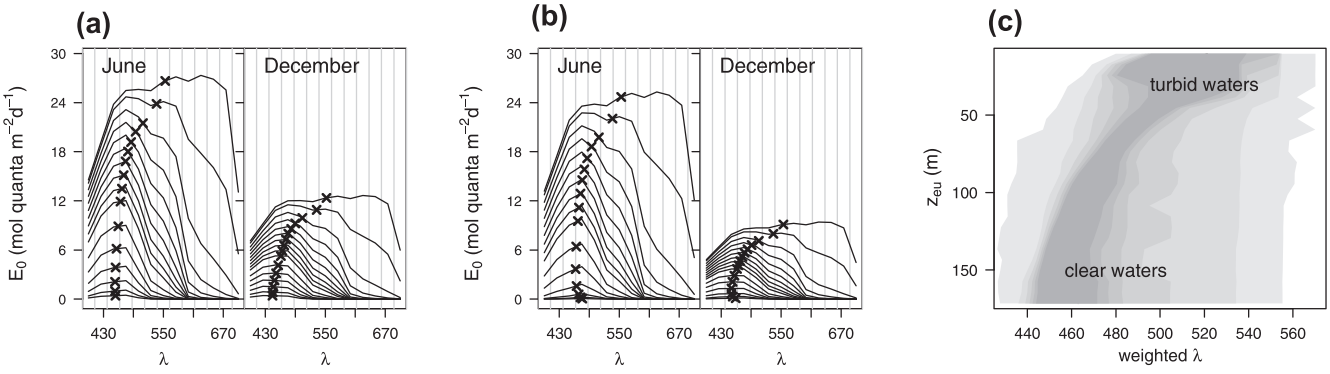

Fig. 8. Light habitats simulated in the Mediterranean Sea in EXP-0 and EXP-1: spectral shape of $E_0(\lambda)$ in consecutive layers of the model, from 1.5 to 150 m (i.e., the sequence of black lines) in two example locations in the **(a)** eastern and **(b)** western Mediterranean Sea, the E_0-weighted λ value for each depth is indicated with crosses (it is read in the x-axis); and **(c)** range of light habitats simulated for the Mediterranean Sea based on E_0-weighted λ and z_{eu}.

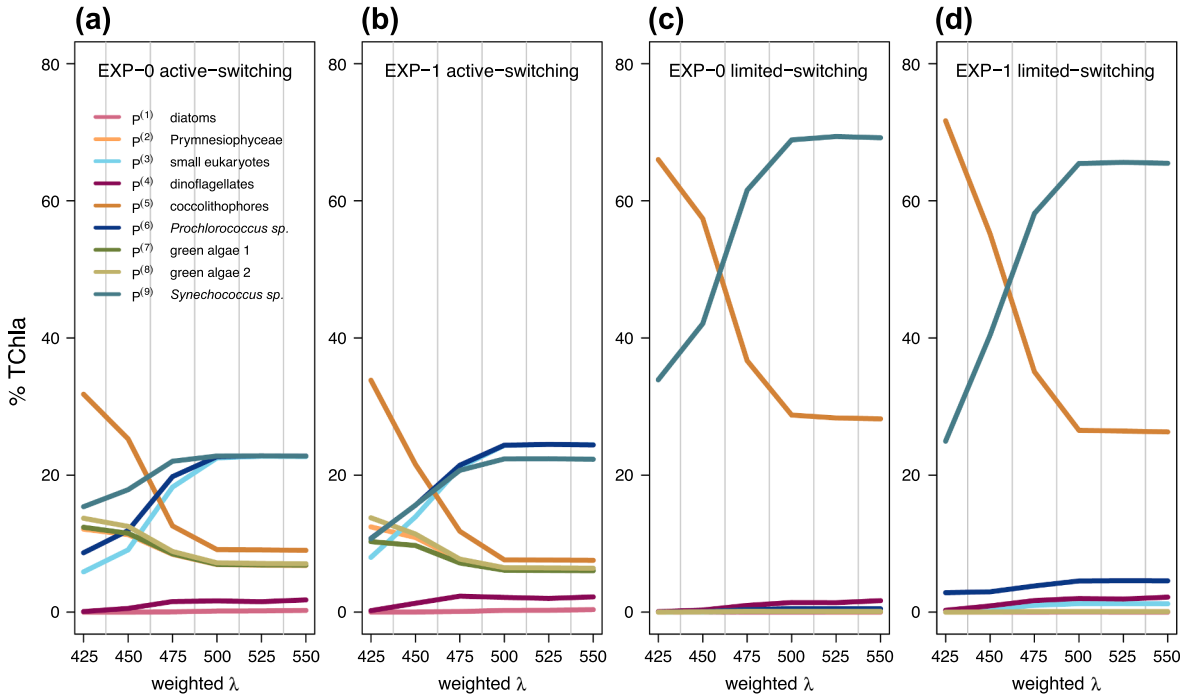

Fig. 9. Proportion of total chlorophyll (TChla) by each PFT as a function of the E_0-weighted λ in **(a)** EXP-0 with active-switching, **(b)** EXP-1 with active-switching, **(c)** EXP-0 with limited-switching and **(d)** EXP-1 with active-switching.

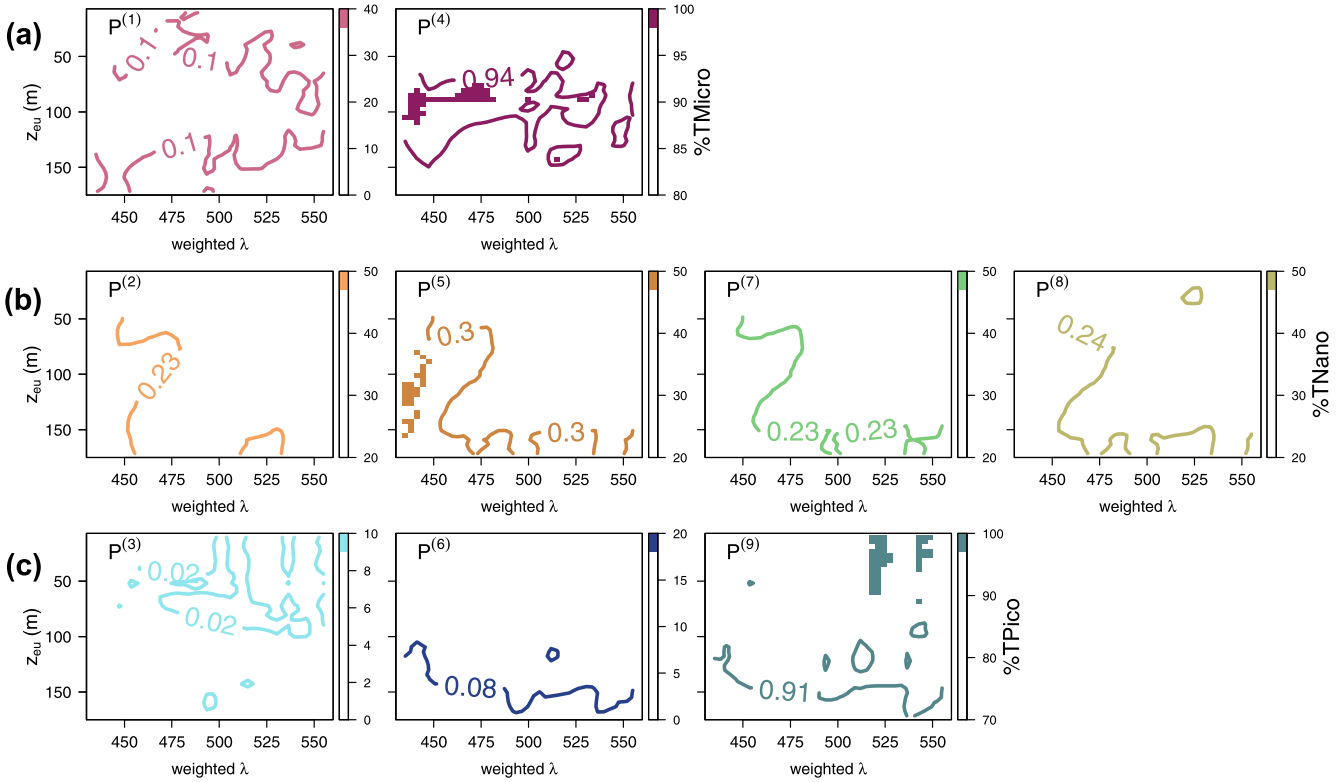

Fig. 10. Preferred water type for each PFT: colour intensity represents the proportion of chlorophyll that each PFT represents within its size class as a function of the E_0-weighted λ and z_{eu}. **(a)** % of $P^{(1)}_{Chl}$ and $P^{(4)}_{Chl}$ in the microphytoplankton chlorophyll and (**b**) % of $P^{(2)}_{Chl}$, $P^{(5)}_{Chl}$, $P^{(7)}_{Chl}$ and $P^{(8)}_{Chl}$ in the nanophytoplankton chlorophyll, both in EXP-1 with active-switching, and **c**) % of $P^{(3)}_{Chl}$, $P^{(6)}_{Chl}$ and $P^{(9)}_{Chl}$ in the picophytoplankton chlorophyll in EXP-1 with limited-switching.

coccolithophores ($P^{(5)}$) within nanophytoplankton and dinoflagellates ($P^{(4)}$) within microphytoplankton throughout the year (Figs. 5 and 6, solid blue lines). The main difference between EXP-0 and EXP-1 under the limited-switching formulation was that, in the latter, coexistence emerged only with changes in $E_0(\lambda)$ (Figs. 5 and 6, dashed blue lines). Changes in the spectral composition of available light, either in time or

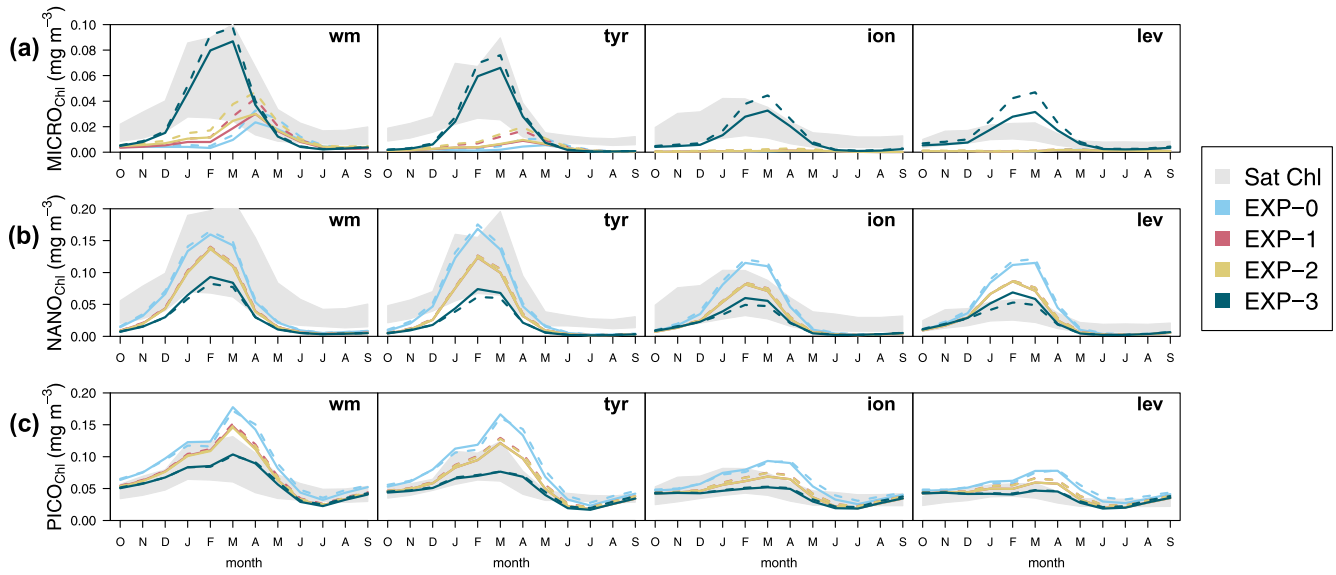

Fig. 11. Temporal evolution of the average chlorophyll concentration at the ocean surface in four major sea basins, the western Mediterranean (wm), Tyrrhenian (tyr), Ionian (ion) and Levantine (lev): (**a**) micro-, (**b**) nano- and (**c**) picophytoplankton size fractions of Chla, observed from satellites (grey area shows the inter-quartile range of values in the basin) and simulated in all experiments. For each experiment, the solid line shows the run that uses the limited-switching grazing formulation, and the dashed line shows the run that uses the active-switching grazing formulation.

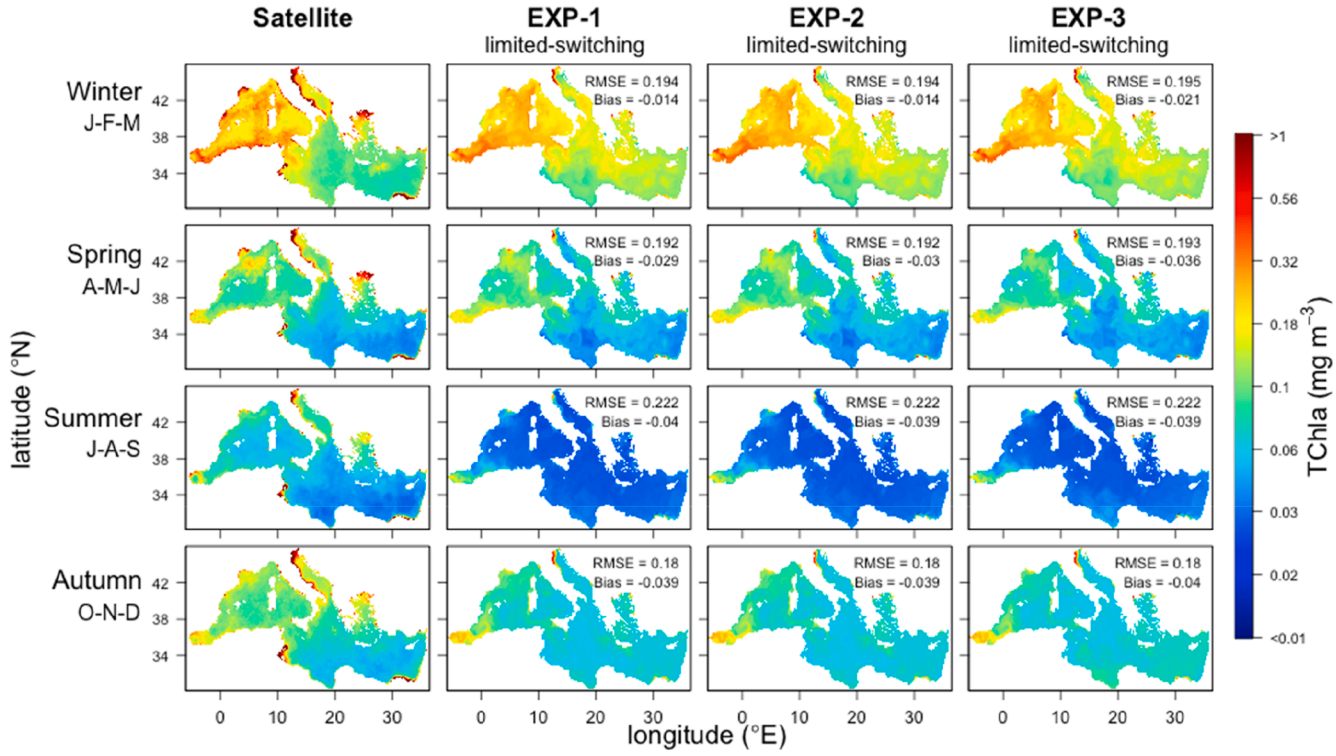

Fig. 12. Seasonal mean maps for the year 2015 of total chlorophyll (TChla) from the satellite product (first column), and from EXP-1 (second column), EXP-2 (third column) and EXP-3 (fourth column), all with the limited-switching grazing formulation. The inserts report the root mean square error (RMSE) and average error (Bias) comparing model simulations to the satellite product for each season.

in space, could reverse the outcome of competition and allow different PFTs to dominate their size class. Indeed, the picophytoplankton size classes $P^{(3)}$ and $P^{(6)}$ were not completely excluded in the easternmost basins, the Ionian basin and the Levantine basin under EXP-1 with limited-switching (Fig. 6). However, a time and/or space variable $E_0(\lambda)$ was not sufficient to generate coexistence in nano- and micro-phytoplankton in either EXP-0 or EXP-1 (Figs. 5 and 6).

3.3. *Light habitats: Coexistence through niche differentiation*

If fluctuations in the spectral composition of $E_0(\lambda)$ can reverse the competitive outcome, what does this tell us about the preferred light habitats of each PFT? To explore which PFTs were able to coexist under different light conditions, we categorized light habitats considering two elements: the depth of the euphotic zone (z_{eu}) (Fig. 7) and the E_0-weighted wavelength, which represents the spectral quality of light with

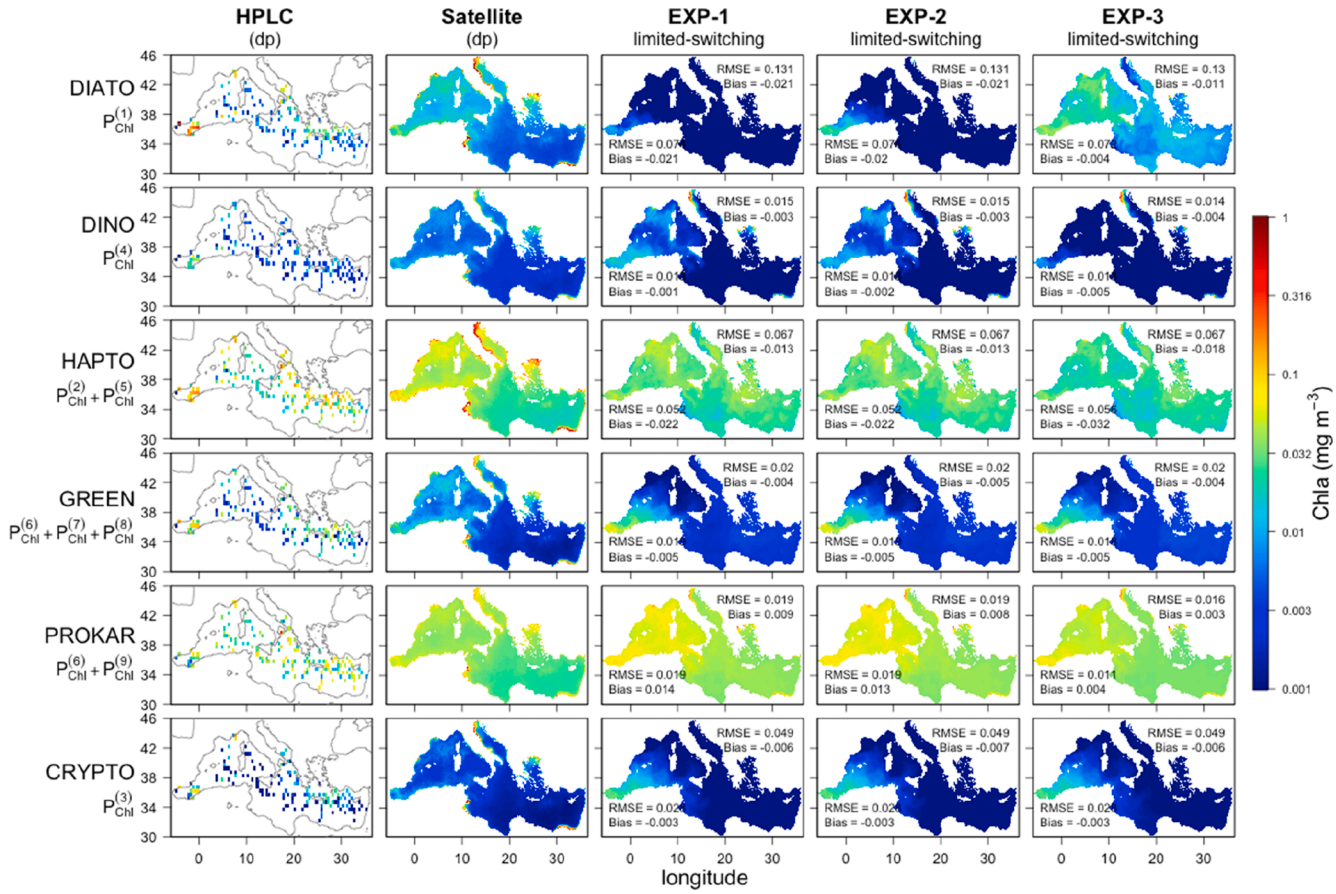

Fig. 13. Annual mean maps for the year 2015 of PFTs chlorophyll from HPLC field data (first column), the satellite product (second column), and from EXP-1 (third column), EXP-2 (fourth column) and EXP-3 (fifth column), all with the limited-switching grazing formulation. Root mean square error (RMSE) and average error (Bias) comparing model simulations to the satellite product for the west and east subbasins are inserted in the left and right parts of the panels, respectively.

a single value that indicates the dominant component of underwater $E_0(\lambda)$. Fig. 8 shows examples of how the shape of $E_0(\lambda)$ changed as it penetrated through the water in two locations of the east (Fig. 8**a**) and west Mediterranean Sea (Fig. 8**b**) in June and December. Given the strong absorption of water in the red portion of the spectrum, the underwater light spectrum narrowed to shorter wavelengths as depth increased. With increasing turbidity, however, the underwater light spectrum shifted towards red. The crosses in Fig. 8**a and b** indicate the E_0-weighted average λ at each depth layer of the model. When combining the E_0-weighted λ down to a 200 m depth with z_{eu}, we can define a space of potential light niches ranging from clear water blue light-dominant and a deep z_{eu} to turbid water red light-dominant with a shallow z_{eu} (Fig. 8**c**). By comparing the water types identified with the contribution of each PFT to TChla and to the chlorophyll of their respective size classes, we explored which PFT succeeded under each particular light habitat.

Given that the E_0-weighted λ covariates with depth and deeper waters were bluer but also richer in nutrients than superficial waters, the match of one PSC to a preferred E_0-weighted λ does not mean that the underwater light spectrum was driven the distribution of that PSC. The proportion of chlorophyll of each PFT as a function of the E_0-weighted λ showed a substitution of nanophytoplankton groups in blue-dominated waters to picophytoplankton with some hints of microphytoplankton in red-dominated waters. However, this reflects only the distribution in depth of the PSCs, with picoplankton dominating more superficial waters than nanoplankton (all panels in Fig. 9). For PFTs within a given PSC, however, opportunities for coexistence arising from light niche differentiation were observed.

Within picophytoplankton, with active-switching, the three PFTs tended to coexist. Whereas in the non-spectral EXP-0, *Synechococcus sp.* ($P^{(9)}$) was more concentrated than the others in clearer waters, in spectral EXP-1, all three were equivalent (Fig. 9**a** vs. **9b**). Regarding limited-switching, for the non-spectral EXP-0, only *Synechococcus sp.* ($P^{(9)}$) survived; however, in the spectral EXP-1, *Prochlorococcus* sp. ($P^{(6)}$) and small eukaryotes ($P^{(3)}$) contributed a small proportion of chlorophyll but coexisted with *Synechococcus sp.* ($P^{(9)}$) (Fig. 9**c** vs. **9d**). This result can be seen in more detail in Fig. 10**c**, where it is shown how *Prochlorococcus* sp. ($P^{(6)}$) preferred clearer bluer waters, and small eukaryotes ($P^{(3)}$) were present in more turbid waters.

Within nanophytoplankton, coccolithophores ($P^{(5)}$) contributed more to total chlorophyll than did other groups in bluer waters in both EXP-0 and EXP-1 with the active-switching grazing formulation (Fig. 9**a and b**). In intermediate and turbid waters, the PFTs of nanoplankton coexisted more evenly (Fig. 10**b**). In EXP-0 with limited-switching, coccolithophores ($P^{(5)}$) were the only survivors of the nanoplankters, and not even spectral EXP-1 allowed coexistence within this size class (Fig. 9**c and d**).

Within microphytoplankton, dinoflagellates ($P^{(4)}$) outcompeted diatoms in any case ($P^{(1)}$), and only a small proportion survived in the active-switching simulations (Fig. 9**a and b**), predominantly in waters dominated by the red component (Fig. 10**a**). The spectral resolution of EXP-1 did not allow for coexistence within this size class (Fig. 9**d**), which made sense given the small difference in terms of the $a^*_{PS}(\lambda)$ of these two types.

3.4. Optical and functional differences among PFTs

In nature, PFTs of a particular size differ not only in their $a^*_{PS}(\lambda)$ but

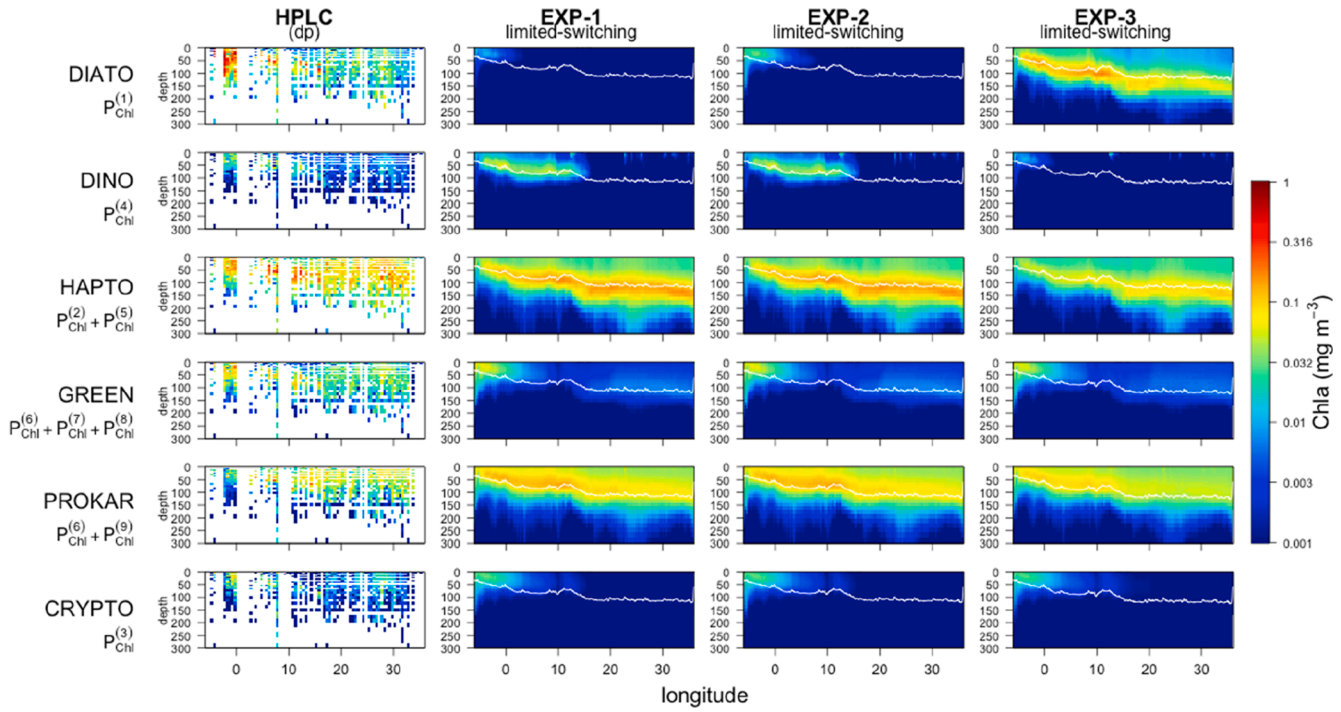

Fig. 14. Annual mean depth profiles (2015) of PFTs chlorophyll from HPLC field data (first column) and from EXP-1 (second column), EXP-2 (third column) and EXP-3 (fourth column), all with the limited-switching grazing formulation. The solid white line shows the euphotic depth (z_{eu}) defined as the depth with 1% of the PAR at the surface.

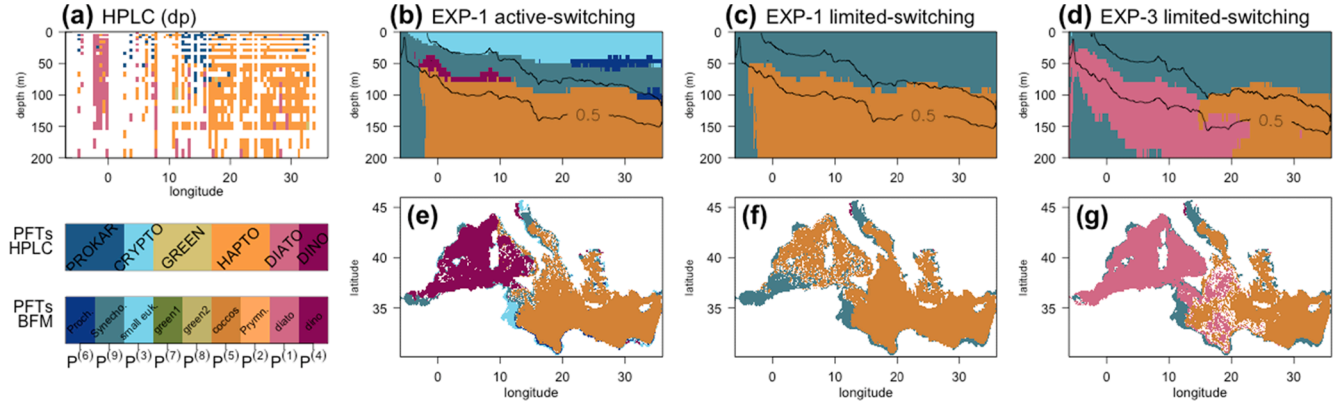

Fig. 15. Most frequently dominant PFT: profiles in depth from **(a)** HPLC field data and from EXP-1 with **(b)** active-switching and **(c)** limited-switching grazing formulation and **(d)** EXP-3 with limited-switching grazing formulation. The solid black line in **b-d** shows the isoline of 0.5 mg m^{-3} of TChla to follow the position of the upper and lower depths of the subsurface chlorophyll maximum layer. For the same model experiments, lower panels **(e, f, g)** show the most frequently dominant PFTs at the depth of the subsurface chlorophyll maximum value (DCM).

also in other traits related to nutrient and light utilization, temperature regulation, sinking behaviour or susceptibility to predation. All PFTs considered as 'brown algae' were relatively similar in their absorption capabilities and were not separated clearly by clustering analysis (Fig. 1). Therefore, in EXP-2 and EXP-3, we introduced some differences in their functional characteristics (Table 3). The outcome of the competition among PFTs in EXP-2 and EXP-3 was the result of their increased functional diversity, diminishing the effect of any potential difference in light-harvesting traits. In any case, the success or coexistence of the group that had a competitive advantage with the others depended on the grazing formulation that maximized competition (limited-switching) or promoted coexistence (active-switching).

In Fig. 11, we summarize all experiments performed in terms of the seasonal evolution of surface chlorophyll in the three PSCs considered. The difference between the use of grazing formulations (solid vs. dashed lines in Fig. 11) was small because the effect occurred within PSCs. Between EXP-1 and EXP-2, there were no differences in the outcome for nanophytoplankton and very few differences in the outcome for microphytoplankton; dinoflagellates were still the dominant group in this size class (see the surface plots in Fig. 13 and the depth profiles in Fig. 14). The large reversal in the competition appeared in EXP-3, where diatoms became far more abundant (see also Fig. 13 and Fig. 14). The increase in photochemical efficiency exacerbated the competitive advantage conferred to otherwise optically similar PFTs. In EXP-3, the chlorophyll of dinoflagellates was minimal, and diatoms were the PFT of large phytoplankton that contributed more to the seasonal evolution of microphytoplankton chlorophyll. Indeed, EXP-3 appeared to be in better agreement with the satellite estimates (Fig. 11**a**). For nano- (Fig. 11**b**) and picophytoplankton (Fig. 11**c**), even if they were not significantly modified in EXP-3 with respect to previous experiments, their total

Table B1
Phytoplankton parameters.

Parameter	Description	Units	$P^{(1)}$ $P^{(4)}$	$P^{(2)}$ $P^{(5)}$ $P^{(7)}$ $P^{(8)}$	$P^{(3)}$ $P^{(6)}$ $P^{(9)}$
			Micro	**Nano**	**Pico**
Q_{10}^{P}	temperature Q10 coefficient	–	2	2	2
ct_P	cut-off threshold for temperature factor	–	0	0	0.75
$Qmin_N$	minimum quotum N:C	mmolN mgC^{-1}	6.87e-3	6.87e-3	6.87e-3
$Qopt_N$	reference quotum N:C	mmolN mgC^{-1}	1.26e-2	1.26e-2	1.26e-2
$Qmin_P$	minimum quotum P:C	mmolP mgC^{-1}	4.288e-4	4.288e-4	4.288e-4
$Qopt_P$	reference quotum P:C	mmolP mgC^{-1}	7.86e-4	7.86e-4	7.86e-4
$Qmin_{Si}$	minimum quotum Si:C	mmolSi mgC^{-1}	0	0	0
$Qopt_{Si}$	reference quotum Si:C	mmolSi mgC^{-1}	0	0	0
$r0_P$	maximal productivity at 10C and nutrient-replete conditions	d^{-1}	1.5	3	3.5
b_P	respiration rate at 10C	d^{-1}	0.1	0.05	0.1
γ_P	activity respiration fraction	–	0.1	0.1	0.2
β_P	excreted fraction of primary production	–	0.15	0.1	0.1
θmax_P	reference quotum Chla:C	mgChl mgC^{-1}	0.02	0.02	0.02
$dChl_P$	turnover rate for Chla	d^{-1}	0.2	0.2	0.2
ϕ	quantum yield	mgC^{-1} µmol $quanta^{-1}$	4.8e-4	4.8e-4	4.8e-4
PIC:POC	reference PIC:POC ratio	mg:mg	0	0.3	0
$\omega sink$	maximum sinking velocity	m d^{-1}	2.5	0	0
$lsink$	nutrient stress threshold for sinking	–	0.75	–	–

contribution to the community was reduced after the increase in microphytoplankton.

3.5. How optical diversity affects PFTs distribution: Comparison to observations.

In the next section, we explore how our model results compare with real-world observations regarding the spatial heterogeneity of the phytoplankton community in the Mediterranean Sea. Model simulated concentrations of TChla at surface (Fig. 12) that, although tended to be smaller than those retrieved by satellite (bias ranged from −0.04 mg m^{-3} in Summer to −0.014 mg m^{-3} in Winter), reproduced dominant seasonal patterns in TChla. No substantial differences are shown by the different optical configurations within a given grazing formulation, highlighting how the light niche description improves the phytoplankton community representation leaving almost unchanged the total chlorophyll. PFTs determined from diagnostic pigments (both for HPLC and for satellite observations) were not fully directly comparable to the modelled PFTs (Table 1). To allow for comparison, we assumed that the DIATO group was comparable to $P^{(1)}$, the DINO group was comparable to $P^{(4)}$, the GREEN group was comparable to the sum of $P^{(6)}$, $P^{(7)}$ and $P^{(8)}$, the HAPTO group was comparable to the sum of $P^{(2)}$ and $P^{(5)}$, the PROKAR group was comparable to the sum of $P^{(6)}$ and $P^{(9)}$, and the CRYPTO group was comparable to $P^{(3)}$ (Table 1). Note that *Prochlorococcus* sp. ($P^{(6)}$) participated in both GREEN and PROKAR; and that $P^{(3)}$ accounted for small eukaryotes, however, in the Mediterranean Sea, Cryptophyceae was the main component of small eukaryotes (DiCicco et al., 2017), which made $P^{(3)}$ and CRYPTO relatively comparable.

Model results compared very well with the observed distributions of phytoplankton from field sampling and satellite with the dominance of PROKAR and HAPTO in most of the Mediterranean Sea, and DIATO reached higher annual averaged chlorophyll than did DINO (Fig. 13). In EXP-1 model simulations, the HAPTO group was formed entirely by coccolithophores ($P^{(5)}$), with negligible contributions of non-calcifying Haptophyta ($P^{(2)}$). Green algae ($P^{(7)}$ and $P^{(8)}$) and small eukaryotes ($P^{(3)}$) were virtually absent, and their concentration in the westernmost part was promoted by the prescribed boundary conditions and the high level of nutrient concentrations in the Alboran subbasin. Within microphytoplankton, dinoflagellates ($P^{(4)}$) were restricted to the western part of the basin and to some spots in the Adriatic and Aegean Seas, whereas diatoms ($P^{(1)}$) were also virtually absent. Within picoplankton, however, other groups were not completely excluded, and there was a general spatial overlap of phytoplankton groups. The PROKAR group in the model simulation was formed mostly by *Synechococcus* sp. ($P^{(9)}$), with contributions of *Prochlorococcus* sp. ($P^{(6)}$). *Prochlorococcus* sp. was particularly concentrated in the eastern part of the basin, as observed in the GREEN group. Accordingly, there was a west-east gradient of *Synechococcus* sp. chlorophyll as *Prochlorococcus* sp. became progressively more concentrated in the east. The same type of distribution was observed in the latitudinally averaged depth profiles (Fig. 14). As seen before, the inclusion of functional differences between diatoms and dinoflagellates in EXP-2 did not noticeably change the distributions, but diatoms increased their chlorophyll, and their general distribution was in better agreement with the observations in EXP-3 (Figs. 13 and 14).

To determine the dominant PFTs in the observations and in the 3D simulations, for each point in space and time, we first computed the PFT that most contributed to TChla and then identified which was the most abundant during more months of the year. Fig. 15 shows the most frequently dominant PFT in the depth and horizontal sections. Even though the dominant PFTs based on observations were affected by the poor temporal coverage of the sampling, PROKAR appeared as the dominant group in superficial waters, HAPTO was dominant in deeper waters and DIATO was dominant in western areas **(**Fig. 15**a).** In the surface of the EXP-1 simulations, a single PFT dominated throughout the year, and the dominant groups were always small eukaryotes ($P^{(3)}$) in the active-switching simulation and *Synechococcus* sp. ($P^{(9)}$) in the limited-switching simulation. In the water column, instead, the gradients in the spectral composition of light led to different groups in different parts of the water column. EXP-1 with active-switching simulation permitted that all picoplankton PFTs were dominant in separate areas of the water column, since the dominant group enlightened its slight competitive advantage under the specific prevailing light conditions. Indeed, small eukaryotes ($P^{(3)}$) dominated at the surface of the Mediterranean Sea, showing their preference for less blue waters. Below they were substituted by *Synechococcus* sp. ($P^{(9)}$), with some spots of *Prochlorococcus sp*. ($P^{(9)}$) in the eastern part (Fig. 15**b**). Within nanoplankton, in contrast, coccolithophores ($P^{(5)}$) were the dominant nanoflagellates in all cases. Microphytoplankton were represented by dinoflagellates ($P^{(4)}$) that were located preferentially at the depth of the subsurface chlorophyll maximum value (DCM) of the western part of the Sea (Fig. 15**e**). In EXP-1 with limited-switching, *Synechococcus* sp. ($P^{(9)}$) was always the dominant group within picoplankton, and coccolithophores ($P^{(5)}$) were dominant within nanoplankton. In this configuration, their distribution simply represented the dominance of picoplankton above the 50 to 80 m depth, extending deeper eastward, and the dominance of nanophytoplankton below that depth (Fig. 15**c**). The depth of exchange between both groups was within the subsurface

Table B2
Zooplankton parameters.

Parameter	Description	Units	$Z^{(6)}$	$Z^{(5)}$	$Z^{(4)}$	$Z^{(3)}$
Q_{10}^{Z}	Q10 value for physiological rates	–	2	2	2	2
$r0_Z$	potential specific growth rate at 10 °C	d^{-1}	5	2	2	2
h_Z	half-saturation food concentration for Type II	mgC m^{-3}	100	30	100	250
$f_{min}^{(1,4)}$	half-saturation food concentration for capturing microphytoplankton	mgC m^{-3}	50	50	0	0
$f_{min}^{(2,5,7,8)}$	half-saturation food concentration for capturing nanophytoplankton	mgC m^{-3}	12.5	12.5	0	0
$f_{min}^{(3,6,9)}$	half-saturation food concentration for capturing picophytoplankton	mgC m^{-3}	16.6	16.6	0	0
δ_B	availability of bacteria	–	1	0.1	–	–
$\delta_P^{(1)}$	availability of diatoms	–	0	0.7	1	0
$\delta_P^{(2,5,7,8)}$	availability of nanophytoplankton	–	0.2	1	0.75	0
$\delta_P^{(3,6,9)}$	availability of picophytoplankton	–	1	0.1	0	0
$\delta_P^{(4)}$	availability of dinoflagellates	–	0	0.1	1	1
$\delta_Z^{(6)}$	availability of nanoheterotrophs	–	0.2	1	0	0
$\delta_Z^{(5)}$	availability of microzooplankton	–	0	1	1	0
$\delta_Z^{(4)}$	availability of omnivorous mesozooplankton	–	0	0	1	1
$\delta_Z^{(3)}$	availability of carnivorous mesozooplankton	–	0	0	0	1
d_Z	specific mortality rate	d^{-1}	0	0	0.02	0.02
dO_Z	oxygen-dependent mortality rate	d^{-1}	0.05	0.05	0.01	0.01
η_Z	assimilation efficiency	–	0.3	0.5	0.6	0.6
β_Z	excreted fraction of uptake	–	0.5	0.5	0.35	0.3
hO_Z	half saturation oxygen for mortality	mmolO_2 m^{-3}	8	8	30	30
γ_Z	exponent for density-dependent mortality	–	–	–	2	2
εc_Z	particulate fraction of excretion	–	0.6	0.6	1	1

Table B3
Bacteria parameters.

Parameter	Description	Units	B
Q_{10}^{B}	Q10 value for physiological rates	–	2.95
$r0_B$	potential specific growth rate at 10 °C	d^{-1}	8.38
ν_B^{R1}	specific potential uptake for labile DOC	d^{-1}	0.5
ν_B^{R2}	specific potential uptake for semi-labile DOC	d^{-1}	0.25
ν_B^{R6}	specific potential uptake for POC	d^{-1}	0.1
$Qopt_N$	optimal N to C quontum	mmolN mgC^{-1}	0.017
$Qopt_P$	optimal P to C quontum	mmolP mgC^{-1}	0.0085

chlorophyll maximum layer (layer identified by the upper and lower isosurface of 0.5 mg Chl m^{-3}) in the west, so the DCM was represented by both groups. In the east, exchange occurred above the upper limit of the subsurface chlorophyll maximum layer; hence, the DCM was dominated by nanoplankton (Fig. 15**f**). In EXP-3 with limited-switching, the distributions of *Synechococcus* sp. ($P^{(9)}$) and coccolithophores ($P^{(5)}$) were similar to those in EXP-1, with the difference that diatoms ($P^{(1)}$) became dominant in the westernmost part of the Sea, substituting dinoflagellates ($P^{(4)}$) (Fig. 15**d**) and representing the dominant group in the DCM of that part of the basin (Fig. 15**g**).

4. Discussion

The light absorption traits of the PFTs present in the Mediterranean Sea and their adaptation to the prevailing light conditions seem to be important factors shaping the spatial heterogeneity and seasonal dynamics of the phytoplankton community in the basin. This finding was revealed by a modelling experiment in which we simulated the underwater spectral light field of the basin and forced optically distinct PFTs to compete in such a virtual environment. While leaving the total chlorophyll substantially not modified (Fig. 12), by considering non-spectrally resolved optical differences among PFTs (EXP-0), our model results led to the dominance of *Synechococcus* sp. ($P^{(9)}$) within picophytoplankton, coccolithophores ($P^{(5)}$) within nanophytoplankton and dinoflagellates ($P^{(4)}$) within microphytoplankton throughout the year. Although the inclusion of the spectral dependency of photosynthesis (EXP-1) allowed the coexistence of picoplanktonic groups, it did not allow the coexistence of nano- and microphytoplanktonic groups. By considering differences in other functional traits (EXP-3), we obtained PFT distributions that were in relative agreement with the observed phytoplankton distributions in the Mediterranean Sea. This result suggests that whereas optical and functional traits are both important in organizing the nano- and microphytoplanktonic communities, spectral light gradients can play a predominant role in organizing the picophytoplanktonic community and shaping their spatial heterogeneity and seasonal dynamics.

Regarding picophytoplankton, our results resembled the biogeographical distributions of picoplankton in the Mediterranean Sea observed from field sampling and retrieved by satellite (DiCicco et al., 2017). *Prochlorococcus* sp. and *Synechococcus* sp. coexisted in many regions, but their distributions did not completely overlap; additionally, *Prochlorococcus* sp. was more abundant in the eastern part, while *Synechococcus* sp. was more dominant in the western part. *Prochlorococcus* sp. gradually increased with water clarity, which agreed with previous model results that predicted the dominance of this genus in the competition for light in the clearest oceans (Stomp et al., 2007) and field observations in the Mediterranean Sea that showed this genus was distributed in deeper layers (Yacobi et al., 1995) and with different ecotypes in different parts of the water column (Brunet et al., 2007; Moore et al., 1995).

Our results for the nanophytoplankton showed the dominance of coccolithophores, which agreed with observations about the prevalence of such group in Mediterranean waters (Siokou-Frangou et al., 2010) where they show high diversity (Cros and Fortuño, 2002). However, in the results shown here, it was not possible to differentiate whether the HAPTO group determined by the diagnostic pigments method was formed by coccolithophores or by other Haptophyta. In our model results, even with a grazing formulation that maximized the coexistence of PFTs, coccolithophores were the prevailing nanoflagellates in clearer waters, regardless of the inclusion of the spectral dependency of photosynthesis, which indicated that their high absorption cross-section ($\overline{a_{PS}^{*}}$) gives them some advantage. $\overline{a_{PS}^{*}}$ considered for coccolithophores in this work was in the range of values reported for *Emiliania huxleyi* (Suggett et al., 2007). Our results suggest that light harvesting traits, along with parameters related to nutrients, temperature, salinity (Ignatiades et al., 2009) and to the seawater carbonate system (Oviedo et al., 2015), may be necessary to simulate the coccolithophore distribution in the Mediterranean Sea.

Microphytoplankton were distributed mostly in the western part, making an important proportion of the total phytoplankton chlorophyll in the DCM, and in coastal spots of the Adriatic, Aegean and Levantine

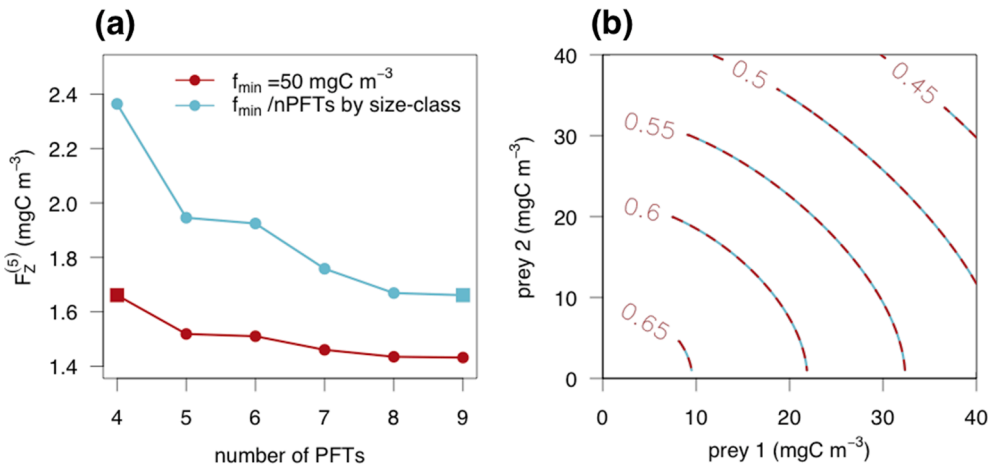

Fig. C1. Behaviour of active-switching functional response for grazing formulation: (**a**) total amount of food available to microzooplankton ($F_Z^{(5)}$) as a function of the number of PFTs in the phytoplankton compartment, (**b**) isoclines of total ingestion of microzooplankton ($I_Z^{(5)}$, mg C m^{-3} d^{-1}) as a function of the biomass of two prey of the same size class (red) and when the same prey are split into four clones each (blue).

subbasins. However, in the EXP-0, EXP-1 and EXP-2 results, diatoms were basically outcompeted by dinoflagellates, which indicated that their small optical differences gave a competitive advantage to dinoflagellates and did not allow for the coexistence of the two PFTs. Differentiating dinoflagellates and diatoms just by their light harvesting traits may be challenging because they exhibit similar spectral absorption and large intraspecific variability (Catlett and Siegel, 2018; Organelli et al., 2017). Observations showed that diatoms were the main contributors to microphytoplankton and formed most of the seasonal blooms in the Mediterranean Sea. This result suggests that their poor performance in terms of light absorption due to the size constraints to pigment packaging (Agustí, 1991) shared with dinoflagellates may be compensated with other competitive traits for light harvesting or light use, such as higher photochemical efficiency (Moore et al., 2005) or higher resistance to photoinhibitory damage (Key et al., 2010). Indeed, when we considered a higher photochemical efficiency for diatoms (EXP-3), they became the most abundant group between these two PFTs, and the model results performed very well with respect to satellite and HPLC observations (Figs. 12 and 13).

The novel configuration of the BFM that was presented in this paper was based on the introduction of a light-harvesting trait in the PFT definition and allowed to simulate 9 different PFTs. The light absorption spectrum result of chromatic adaptation is different among phytoplankton types (Sathyendranath et al., 1987), relatively conservative within types (Organelli et al., 2017) and available from experiments in a relatively large number of phytoplankton taxa (see Appendix A). These characteristics permitted the assignment of a representative spectrum to each PFT using clustering techniques based on the similarities in the light absorption spectra. Such techniques have been demonstrated to be useful for the classification of algal assemblages (Torrecilla et al., 2011; Uitz et al., 2015), the taxonomic discrimination of water samples (e.g., Moberg et al., 2002; Organelli et al., 2017) and the grouping of spectral phytoplankton types in optical models (Xi et al., 2017, 2015). However, the absorption coefficients assigned to a particular PFT were not constant since they comprised several pigment types that have branched out over a wide range of aquatic ecosystems. Light absorption is influenced by pigment content altered by processes of photoacclimation (Pérez et al., 2021) and adaptation (Brunet et al., 2007) that result in phytoplankton groups or ecotypes with variable competitive abilities over time and space. The variability in absorption coefficients can alter the correspondence between light niches and phytoplankton types, and hence, further work is needed to represent such variability in bio-optical models. This raises interesting perspectives to improve the descriptive capacity of spectral light harvesting traits by including their variability in terms of photoacclimation and/or speciation.

By considering PFTs within each size-class equivalent competitors in all functional traits except light absorption, our results showed a significant impact of optical variability on the distribution and dominance of PFTs within picophytoplankton and a smaller impact on the PFTs within nano- and microphytoplankton. Nonetheless, variability in other functional traits, such as those related to resistance to photoinhibition (Six et al., 2007) or those related to nutrient acquisition and use (Mouriño-Carballido et al., 2016), can incorporate another layer of complexity. Species that are defined as strong competitors in one niche dimension can display stable species coexistence if their competitive traits are differentiated across another niche dimension. In this sense, although our analysis is not comprehensive in terms of traits chosen, it does indicate clear model calibration directions fostering and hastening model improvements. Regarding light use, (Luimstra et al., 2020) proposed a competition model where resource acquisition (light absorption) and resource use efficiency (photosynthetic efficiency) of different light colours varied independently. In this case, even when a given species was the stronger competitor absorbing different light colours, coexistence with another species was possible if the latter was more efficient using the absorbed light. Indeed, our EXP-3 showed how diatoms with a higher photochemical efficiency improved the BFM description of the microphytoplankton PFTs. Further work can be done to include other functional variability in the description of PFTs and ultimately increase the model ability to represent the distribution and seasonal dynamics of the phytoplankton community in the Mediterranean Sea.

Despite potential further improvements of the model configuration, the goal of this work was to put optically different groups of phytoplankton in a virtual environment that simulated a realistic range of incoming spectral light. By observing the extent of competition for light under these simulated conditions, our approach and results enlighten potential factors shaping the taxonomic composition of natural phytoplankton communities in marine ecosystems, particularly in the Mediterranean Sea. Bio-optical models that describe the optical properties of the water constituents in detail allow us to simulate the heterogeneity of the spectral underwater light field. This turns the model into a useful laboratory to explore the influence of chromatic adaptation in the competition for light. With this objective, we needed to shape three elements in our modelling framework, each with its own uncertainties when extrapolating modelling results to the real world: i) provide a variety of light niches, ii) define which is the light-use trait that gives the competitive advantage and its variability among groups, and iii) ensure that other phytoplankton traits and mortality (we selected grazing

formulation) allow us to see the result of competition. We have defined niche variability with the underwater light spectrum and the euphotic depth (for a similar niche definition with turbidity and mixed layer depth, see Stomp et al. (2007)). With this definition, superficial red-dominant waters tended to be dominated by *Synechococcus* sp. almost exclusively, whereas deeper and blue-dominant waters tended to offer more opportunities for the coexistence of optically different PFTs. Under clearer light habitats, coccolithophores were particularly abundant throughout the basin, with contributions of *Prochlorococcus* sp. in the less productive eastern part and microphytoplankton in the DCM of the more productive western part. Hence, these results showed different coexistence patterns under different water types or niches, stressing the role of the underwater light spectrum in shaping the distribution of the autotrophic community.

The light spectrum is not only variable depending on the PFTs present in the water but also depends on dissolved organic matter and non-algal and inorganic particles. CDOM and detrital absorption, characterized by a wavelength-dependent exponentially decreasing spectrum, can greatly influence the underwater light spectrum simulated by the model. In our model setup, CDOM is produced mainly as a fraction of phytoplankton exudation and mortality, and hence, its concentration covariates with phytoplankton (not shown). This could not always be the case, especially in the Mediterranean Sea, whose peculiar optical properties are often attributed to the contribution of CDOM (Volpe et al., 2007) and different parameterizations of the CDOM cycle impact the inherent and apparent optical properties simulated for the basin (Lazzari et al., 2021a). The lack of covariance between bio-optical components and the strong absorption of CDOM in the blue part of the spectrum are confounding elements (Sauer et al., 2012) that can shift the light spectrum to longer wavelengths, more than our simulations showed. Thus, the still unclear changes in dissolved material caused by changes in anthropogenic activities and climate change (Wagner et al., 2020) may influence the phytoplankton community structure as a result of competition for light. Moreover, we have not considered the influence of other particles, such as bacteria (Stramski and Kiefer, 1998) or zooplankton (Davies et al., 2021).

Caveats in the simulation of the variability of light habitats could explain some discrepancies in model results when compared to observations. Within picophytoplankton, our model simulations predicted a negligible contribution of cryptophytes, but observations showed that they contributed more to the phytoplankton community in the Mediterranean Sea. The pigmentation of cryptophytes is well suited for photosynthesis in superficial and/or turbid waters, as they can exploit the green and orange-red part of the light spectrum (Cunningham et al., 2019; Luimstra et al., 2020). The competitive exclusion of cryptophytes in our model simulations can be caused by an underestimation of CDOM in our simulations that, if present, would shift the light spectrum to red, creating appropriate niches for the coexistence of this group.

Altogether, the results presented support the idea that changes in community composition can be driven, to a significant extent, by changes in the available light niches. Hence, radiative transfer models that simulate spectral light habitats seem to be valuable tools that can be used to improve simulations of the biogeography of primary producers (Holtrop et al., 2021). This result is relevant in the ocean surface, where our integrated optical-biogeochemical approach could help to provide insights into how changes in phytoplankton composition influence the optical properties of the ocean that are retrieved by satellites. However, given the strong vertical variability of the light spectrum, this approach would be particularly powerful to simulate accurate phytoplankton distributions in depth. The vertical structure of phytoplankton community composition can be very relevant when evaluating carbon fluxes, such as primary production or carbon export. In the Mediterranean Sea, whereas picophytoplankton dominate most of the superficial open ocean waters, the full water-column fluxes would be very influenced by the nano- and microphytoplankton PFTs inhabiting the deeper parts.

5. Conclusions

Mediterranean waters are optically complex and offer a variety of light niches for phytoplankton. PFTs occupy niches based, among others, on their light-harvesting and light-utilization traits. By including competitive differences in absorption cross-sections, our ecosystem model was shown to be able to shape the phytoplankton community composition of the Mediterranean Sea while total chlorophyll remain unchanged and was in good agreement with observations. Changes in picoplanktonic community composition seemed to be driven, to a significant extent, by changes in the available light niches. Within nano- and microplanktonic communities, the opportunities for coexistence provided by different spectral light habitats were lower, and other functional traits should also be considered. Our 9-optical PFT model including diatoms with higher light utilization efficiency reproduced the zonal and vertical gradients of dominant phytoplankton groups in the Mediterranean Sea. Bio-optical models that simulate the spectral component of underwater light fields can be valuable tools used to improve simulations of the diversity and biogeography of primary producers in the ocean.

CRediT authorship contribution statement

Eva Álvarez: Conceptualization, Methodology, Software, Validation, Visualization, Writing – original draft. **Paolo Lazzari:** Conceptualization, Methodology, Software, Writing – review & editing. **Gianpiero Cossarini:** Conceptualization, Methodology, Supervision, Writing – review & editing.

Declaration of Competing Interest

The authors declare that they have no known competing financial interests or personal relationships that could have appeared to influence the work reported in this paper.

Acknowledgements

The Copernicus Marine Environment Monitoring Service (CMEMS) is implemented by Mercator Ocean International within the framework of a delegation agreement with the European Union. This work was performed within the framework of the BIOPTIMOD CMEMS Service Evolution project (66-SECALL2) and the H2020 SEAMLESS project (GA n. 10100403). All simulations were conducted on the GALILEO100 supercomputing facility at CINECA; we acknowledge the CINECA award under the ISCRA initiative (HP10CMKVJ2) for the availability of high-performance computing resources and support. This study has been conducted using E.U. Copernicus Marine Service Information, and datasets available at PANGAEA (hosted by AWI and MARUM) and at SeaBASS (hosted by NASA).

Appendix A:. Supplementary data

We performed a literature review to collect chlorophyll-specific absorption, scatter, and backscatter to total scatter ratio spectra of phytoplankton. For each spectrum, we collected information regarding the species, genera or phytoplankton class from where the spectrum was measured. When available, the code for the strain, the culture collection where the strain was maintained, and the place of isolation were included. Additionally,

information regarding irradiance conditions and mean size of the cells in culture was included when available, although it was not used in the present work. The reference, number of the figure or table from which the spectrum was digitized and the page where the figure or table was located were also recorded.

A total of 214 chlorophyll-specific absorption spectra ($a^*_{PH}(\lambda)$) were digitized and linearly interpolated to 81 wavelengths between 300 and 800 nm. A total of 72 chlorophyll-specific scatter spectra ($b^*_{PH}(\lambda)$) were digitized and linearly interpolated to 35 wavelengths between 412 and 715 nm. Fifty-seven backscatter-to-scatter ratio spectra ($br_{PH}(\lambda)$) were digitized and linearly interpolated to 9 wavelengths between 412 and 715 nm. These three collections of spectra are available in the supplementary files: *absorption_spectra.csv*, *scatter_spectra.csv* and *backscatter_ratio_spectra.csv*.

Although included in the datasets, we flagged and did not use for further analysis spectra when i) a freshwater species was used and ii) when the chlorophyll-specific spectrum was obtained by dividing $a_{PH}(\lambda)$ by the sum of total chlorophyll and phaeopigments instead of only by total chlorophyll (Bricaud et al., 1983; Bricaud and Morel, 1986; Ciotti et al., 2002; Morel, 1987; Sathyendranath et al., 1987; Suggett et al., 2004), which left us with 177 $a^*_{PH}(\lambda)$, 36 $b^*_{PH}(\lambda)$ and 35 $br_{PH}(\lambda)$ spectra for the analysis described in the main text.

Appendix B:. Ecosystem model

The full description of the BFM equations can be found in the BFM manual (Vichi et al., 2015). Here, we report equations related to the source and loss terms of optically active biogeochemical products that complete the differential equations reported in the main text.

Temperature regulation

The effect of temperature regulating physiological processes is parameterized in a nondimensional form (et_P for phytoplankton, et_Z for zooplankton, et_B for bacteria and et_C for CDOM). The Q_{10} coefficient is different for processes related to phytoplankton (Q^P_{10}, Table B1), zooplankton (Q^Z_{10}, Table B2), bacteria (Q^B_{10}, Table B3) and CDOM (Q^C_{10}, Table 2).

$$et = Q_{10}{}^{(T-10/10)} \tag{B1}$$

In phytoplankton, a cut-off value (ct_P) applied to the temperature regulating factor controls the growth of picophytoplankton at high latitudes.

$$et_P^{(i)} = \max\left(0, et - ct_P^{(i)}\right);\ \mathrm{i} = 1 \text{ to } 9 \tag{B2}$$

Nutrient limitations

All nutrient limitations are dependent on the internal quota of nutrients with respect to C (Q_N, Q_P and Q_{Si}). The minimum allowed quota ($Qmin_N$, $Qmin_P$ and $Qmin_{Si}$) represents the adaptation of each plankton type to the prevailing nutrient concentrations and the optimal quota ($Qopt_N$, $Qopt_P$ and $Qopt_{Si}$) indicates the cellular requirement for optimal growth. Multi-nutrient limitations are computed using Liebig's law of the minimum.

Phytoplankton growth is limited only by non-storable nutrients (fg_P), hence the internal quota of Si when a Si dependency is prescribed. Chlorophyll synthesis is limited by the most limiting term between N and P (fnp_P) and phytoplankton sinking is regulated by the most limiting among the three nutrients (ft_P). The minimum and optimal quotas for phytoplankton are reported in Table B1.

$$fg_P^{(i)} = \min\left(1, \max\left(0, \frac{Q_{Si} - Qmin_{Si}}{Qopt_{Si} - Qmin_{Si}}\right)\right) \tag{B3}$$

$$fnp_P^{(i)} = \min\left(\frac{Q_N - Qmin_N}{Qopt_N - Qmin_N}, \frac{Q_P - Qmin_P}{Qopt_P - Qmin_P}\right) \tag{B4}$$

$$ft_P^{(i)} = \min\left(fg_P^{(i)}, fnp_P^{(i)}\right) \tag{B5}$$

Bacterial uptake of dissolved and particulate substrates is limited by their internal quota of P and N (fnp_B) and by the quality of the labile dissolved substrate (fnp_{R1}) and the particulate substrate (fnp_{R6}). The optimal quotas for bacteria are reported in Table B3.

$$fnp_B = \min\left(1, \frac{B_P/B_C}{Qopt_P}, \frac{B_N/B_C}{Qopt_N}\right) \tag{B6}$$

$$fnp_{R1} = \min\left(1, \frac{R_P^{(1)}/R_C^{(1)}}{Qopt_P}, \frac{R_N^{(1)}/R_C^{(1)}}{Qopt_N}\right) \tag{B7}$$

$$fnp_{R6} = \min\left(1, \frac{R_P^{(6)}/R_C^{(6)}}{Qopt_P}, \frac{R_N^{(6)}/R_C^{(6)}}{Qopt_N}\right) \tag{B8}$$

B1. Phytoplankton

Exudation

Total exudation by phytoplankton (d^{-1}) accounts for the fraction of photosynthesized carbon that cannot be assimilated into biomass and is released in the form of semi-labile dissolved carbohydrates (R^2_C). It is the sum of an activity exudation linked to the gross primary production and a

balance term that accounts for which fraction of fixed C cannot be used for growth given the internal storage of N and P and is excreted.

$$exudation_P^{(i)} = activityexudation_P^{(i)} + nutrientstressexudation_P^{(i)}; i = 1to9 \quad \text{(B9)}$$

Nutrient-stress exudation contributes to the semi-labile DOC pool with no CDOM considered in it, which implies assuming that those carbohydrates excreted under N and/or P shortages are transparent. Details about the formulation of the nutrient-stress exudation can be found elsewhere (Lazzari et al., 2012; Vichi et al., 2015, 2004).

Activity excretion (d^{-1}), on the other hand, is a fraction (β_P) of photosynthesis and contributes 2% of CDOM, as indicated in the main text:

$$activityexudation_P^{(i)} = \beta_P^{(i)} \times photosynthesis_P^{(i)}; \mathrm{i} = 1 \text{ to } 9 \quad \text{(B10)}$$

Respiration

Respiration (d^{-1}) is computed as the sum of the activity respiration computed as a fraction (γ_P) of the photosynthesis minus activity exudation and the basal respiration rate (b_P), temperature dependent and independent of the production rate.

$$respiration_P^{(i)} = \gamma_P^{(i)} \times (photosynthesis_P^{(i)} - activityexudation_P^{(i)}) + b_P^{(i)} \times et_P^{(i)}; \mathrm{i} = 1 \text{ to } 9 \quad \text{(B11)}$$

Calcification

The production of PIC by phytoplankton is controlled by the PIC:POC ratio, which is regulated by nutrients, temperature and density. However, we have not described any particular optical properties for the PIC, and in our setup, only alkalinity was impacted. The PIC:POC production ratio is 0.3 for all nanophytoplankton.

B2. Zooplankton

Microzooplankton: excretion of CDOM and POC

The excretion by zooplankton (mgC m^{-3} d^{-1}) is the sum of the activity excretion and the mortality. Activity excretion is proportional to total ingestion ($I_Z^{(j)}$) multiplied by the assimilation efficiency (η_Z) and the fraction of uptake that is excreted (β_Z). Mortality is parameterized as senescence with a first-order rate based on a constant mortality rate (d_Z) and an oxygen-regulated component (dO_Z).

$$excretion_Z^{(j)} = I_Z^{(j)} \times \eta_Z^{(j)} \times \beta_Z^{(j)} + \left(1 - \frac{O_2}{O_2 + hO_Z^{(j)}}\right) \times dO_Z^{(j)} \times Z_C^{(j)} + d_Z^{(j)} \times Z_C^{(j)}; \mathrm{j} = 5,6 \quad \text{(B12)}$$

Total excretion is partitioned to DOC ($R_C^{(1)}$) and to POC ($R_C^{(6)}$) by the parameter εc_Z as indicated in the main text.

Mesozooplankton: excretion of POC

In addition to the first-order rate of mortality and the oxygen-regulated component, mesozooplankton have a grazing closure by higher trophic levels not resolved in the model, which is a power function of density.

$$excretion_Z^{(j)} = I_Z^{(j)} \times \beta_Z^{(j)} + \left(1 - \frac{O_2}{O_2 + hO_Z^{(j)}}\right) \times et_Z^{(j)} \times dO_Z^{(j)} \times Z_C^{(j)} + d_Z^{(j)} \times Z_C^{(j)^{\gamma_Z^{(j)}}}; \mathrm{j} = 3,4 \quad \text{(B13)}$$

Total excretion by mesozooplankton (mgC m^{-3} d^{-1}) only contributes to POC ($R_C^{(6)}$).

B3. Bacteria

Consumption of CDOM and POC

The main source of carbon for bacterioplankton is the organic matter pool, which is composed of particulate detritu ($R^{(6)}$) and dissolved organic matter ($R^{(1)}$ and $R^{(2)}$). The carbon component of the latter now includes chromophoric ($R_l^{(1)}$ and $R_l^{(2)}$) and non-chromophoric compounds ($R_C^{(1)}$ and $R_C^{(2)}$). The total uptake rate of dissolved and particulate substrates by bacteria (I_B, mg C m^{-3} d^{-1}) is computed as the minimum between the potential uptake and the realized uptake, the latter is dependent on the type of substrates available and their quality.

$$potential\ uptake = fnp_B \times et_B \times r0_B \times B_C \quad \text{(B14)}$$

$$realized\ uptake = \nu_B^{R1} \times fnp_{R1} \times \left(R_C^{(1)} + R_l^{(1)}\right) + \nu_B^{R2} \times \left(R_C^{(2)} + R_l^{(2)}\right) + \nu_B^{R6} \times fnp_{R6} \times R_C^{(6)} \quad \text{(B15)}$$

$$I_B = \min(potential\ uptake,\ realized\ uptake) \quad \text{(B16)}$$

The uptake rate (mgC m^{-3} d^{-1}) of each particular substrate is then proportional to the contribution of that substrate to the total available food. Here we specify the uptake rates of CDOM (*uptakeR1l* and *uptakeR2l*) and NAP (*uptakeR6c*), but the expressions for all other substrates are equivalent.

$$uptakeR1l = I_B \times \frac{\nu_B^{R1} \times fnp_{R1} \times R_l^{(1)}}{realizeduptake} \quad \text{(B17)}$$

$$uptakeR2l = I_B \times \frac{\nu_B^{R2} \times R_l^{(2)}}{realizeduptake} \tag{B18}$$

$$uptakeR6c = I_B \times \frac{\nu_B^{R6} \times fnp_{R6} \times R_C^{(6)}}{realizeduptake} \tag{B19}$$

B4. Sinking

Both detritus and phytoplankton sink with a constant background sinking rate (5 m s^{-1} for non-algal particles and phytoplankton below 150 m). Additionally, phytoplankton sink at a dynamic sinking velocity that is dependent on nutrient stress. The dynamic sinking velocity reaches its maximum ($\omega sink$) as ft_P (nutrient regulation factor) decreases below a threshold ($lsink$) (Table B1).

$$sinking_P^{(i)} = \omega sink^{(i)} \times \max\left(0, lsink^{(i)} - ft_P^{(i)}\right);\ \mathrm{i} = 1,4 \tag{B20}$$

For a complete description of the processes not described here and a comprehensive list of parameter values, see the supplementary material of Lazzari et al. (2012).

Appendix C:. Subdivision of phytoplankton groups

The choice of the grazing response has already been shown to drastically change the simulated distributions of phytoplankton biogeography (Anderson et al., 2010) and diversity (Prowe et al., 2012). Active-switching functional responses present some inconsistencies when dealing with variable numbers of prey (Anderson et al., 2010; Vallina et al., 2014). The formulation of active-switching used in the BFM results in suboptimal feeding, a phenomenon where total ingestion decreases even though total prey biomass stays constant (Fig. 3**A**, red) when more nutritious resources become relatively rarer (Gentleman et al., 2003) as a result of food classes being subdivided (Visser and Fiksen, 2013). In the BFM, this happens because the total available food for a given predator ($F_Z^{(j)}$, Eq. (26)) decreases even though total prey biomass stays constant, as the phytoplankton compartment is subdivided into more PFTs (Fig. C1**a**, red).

To avoid this behaviour and with the aim of keeping $F_Z^{(j)}$ independently if the total prey biomass was divided into 4 PFTs as former applications of the BFM do or in 9 PFTs as this work does, we adjusted the value of $f_{min}^{(i)}$ (Fig. C1**a**, blue). In practice, this means that the minimum size of the prey patches detectable and grazed by the predator is proportionally smaller as the biomass of a particular size class is split into decreasingly abundant PFTs. Picophytoplankton was divided into three PFTs, and $f_{min}^{(3,6,9)}$ was decreased from 50 to 16.6 mg m^{-3}. Nanophytoplankton was divided into four PFTs, and $f_{min}^{(2,5,7,8)}$ was decreased from 50 to 12.5 mg m^{-3}. For microphytoplankton, since $P^{(1)}$ and $P^{(4)}$ were already separated in previous applications of BFM, $f_{min}^{(1,4)}$ was kept at 50 mg m^{-3} (Table B2 in **Appendix B**). With this parameter value update, the model behaviour was consistent with 4 or 9 PFTs in terms of $F_Z^{(j)}$ (Fig. C1**a**, red vs. blue square) and $I_Z^{(j)}$ (Fig. C1.**b**, red vs. blue curves), respectively.

Note here that this is not presented as a general solution to overcome inconsistencies in the active-switching formulations dealing with variable numbers of PFTs but as a parameter value adjustment to maintain model behaviour when changing a state-of-the-art BFM configuration with 4 PFTs to one configuration with 9 PFTs. Other formulations that combine active-switching with maximum feeding, such as that in Vallina et al. (2014), could allow the intercomparability of model simulations with a variable number of PFTs and the building of clone-consistent models (Ansmann and Bollenbach, 2021).

Appendix C. Supplementary material

Supplementary data to this article can be found online at https://doi.org/10.1016/j.pocean.2022.102789.

References

Aas, E., 1987. Two-stream irradiance model for deep waters. Appl. Optics 26, 2095–2101. https://doi.org/10.1364/AO.26.002095.

Ackleson, S.G., Balch, W.M., Holligan, P.M., 1994. Response of water-leaving radiance to particulate calcite and chlorophyll a concentrations: a model for Gulf of Maine coccolithophore blooms. J. Geophys. Res. 99, 7483–7500. https://doi.org/10.1029/93JC02150.

Agustí, S., 1991. Allometric scaling of light absorption and scattering by phytoplankton cells. Can. J. Fish. Aquat. Sci. 48 (5), 763–767. https://doi.org/10.1139/f91-091.

Ahn, Y.-H., Bricaud, A., Morel, A., 1992. Light backscattering efficiency and related properties of some phytoplankters. Deep-Sea Res. 39 (11-12), 1835–1855. https://doi.org/10.1016/0198-0149(92)90002-B.

Aiken, J., Pradhan, Y., Barlow, R., Lavender, S., Poulton, A., Holligan, P., Hardman-Mountford, N., 2009. Phytoplankton pigments and functional types in the Atlantic Ocean: A decadal assessment, 1995–2005. Deep-Sea Res PT II 56 (15), 899–917. https://doi.org/10.1016/j.dsr2.2008.09.017.

Anderson, T.R., Gentleman, W.C., Sinha, B., 2010. Influence of grazing formulations on the emergent properties of a complex ecosystem model in a global ocean general circulation model. Prog. Oceanogr. 87 (1-4), 201–213. https://doi.org/10.1016/j.pocean.2010.06.003.

Ansmann, G., Bollenbach, T., Patil, K.R., 2021. Building clone-consistent ecosystem models. PLoS Comput. Biol. 17 (2), e1008635. https://doi.org/10.1371/journal.pcbi.1008635.

Antoine, D., 2012. Boussole HPLC dataset. SeaBASS. https://doi.org/10.5067/SeaBASS/BOUSSOLE/DATA001.

Babin, M., Morel, A., Claustre, H., Bricaud, A., Kolber, Z., Falkowski, P.G., 1996. Nitrogen- and irradiance-dependent variations of the maximum quantum yield of carbon fixation in eutrophic, mesotrophic and oligotrophic marine systems. Deep-Sea Res PT I 43 (8), 1241–1272. https://doi.org/10.1016/0967-0637(96)00058-1.

Baird, M.E., Cherukuru, N., Jones, E., Margvelashvili, N., Mongin, M., Oubelkheir, K., Ralph, P.J., Rizwi, F., Robson, B.J., Schroeder, T., Skerratt, J., Steven, A.D.L., Wild-Allen, K.A., 2016. Remote-sensing reflectance and true colour produced by a coupled hydrodynamic, optical, sediment, biogeochemical model of the Great Barrier Reef, Australia: Comparison with satellite data. Environ Modell Softw 78, 79–96. https://doi.org/10.1016/j.envsoft.2015.11.025.

Baretta-Bekker, J.G., Baretta, J.W., Hansen, A.S., Riemann, B., 1998. An improved model of carbon and nutrient dynamics in the microbial food web in marine enclosures. Aquat. Microb. Ecol. 14, 91–108. https://doi.org/10.3354/ame014091.

Behrenfeld, M., Dall'Olmo, G., 2020. BOUM08 HLPC dataset [WWW Document]. accessed 1.28.21 Behrenfeld_08-74_report-rev121908.sb. https://seabass.gsfc.nasa.gov/archive/OSU/VF/archive.

Bidigare, R.R., Ondrusek, M.E., Morrow, J.H., Kiefer, D.A., 1990. In-vivo absorption properties of algal pigments, in: Proc. SPIE 1302, Ocean Optics X. 1990 Technical

Symposium on Optics, Electro-Optics, and Sensors, Orlando, FL. doi: 10.1117/12.21451.
Bosc, E., Bricaud, A., Antoine, D., 2004. Seasonal and interannual variability in algal biomass and primary production in the Mediterranean Sea, as derived from 4 years of SeaWiFS observations. Global Biogeochem. Cycles 18 (1), n/a–n/a. https://doi.org/10.1029/2003GB002034.
Boss, E., Claustre, H., 2014. TARA-Mediterranean HPLC dataset. SeaBASS. https://doi.org/10.5067/SeaBASS/TARA_MEDITERRANEAN/DATA001.
Boss, E., Claustre, H., 2012. TARA-Oceans-Expedition HPLC dataset. SeaBASS. https://doi.org/10.5067/SeaBASS/TARA_OCEANS_EXPEDITION/DATA001.
Bricaud, A., Bédhomme, A.-L., Morel, A., 1988. Optical properties of diverse phytoplanktonic species: experimental results and theoretical interpretation. J Plank Res 10 (5), 851–873. https://doi.org/10.1093/plankt/10.5.851.
Bricaud, A., Claustre, H., Ras, J., Oubelkheir, K., 2004. Natural variability of phytoplanktonic absorption in oceanic waters: influence of the size structure of algal populations. J. Geophys. Res. 109.
Bricaud, A., Morel, A., 1986. Light attenuation and scattering by phytoplanktonic cells: a theoretical modeling. Appl. Opt. 25, 571–580. https://doi.org/10.1364/AO.25.000571.
Bricaud, A., Morel, A., Prieur, L., 1983. Optical efficiency factors of some phytoplankters. Limnol. Oceanogr. 28, 816–832. https://doi.org/10.4319/lo.1983.28.5.0816.
Brunet, C., Casotti, R., Vantrepotte, V., Conversano, F., 2007. Vertical variability and diel dynamics of picophytoplankton in the Strait of Sicily, Mediterranean Sea, in summer. Mar. Ecol. Prog. Ser. 346, 15–26. https://doi.org/10.3354/meps07017.
Buesseler, K.O., 1998. The decoupling of production and particulate export in the surface ocean. Global Biogeochem. Cycles 12 (2), 297–310. https://doi.org/10.1029/97GB03366.
Burson, A., Stomp, M., Mekkes, L., Huisman, J., 2019. Stable coexistence of equivalent nutrient competitors through niche differentiation in the light spectrum. Ecology 100, e-02873. https://doi.org/10.1002/ecy.
Butenschön, M., Clark, J., Aldridge, J.N., Icarus Allen, J., Artioli, Y., Blackford, J., Bruggeman, J., Cazenave, P., Ciavatta, S., Kay, S., Lessin, G., van Leeuwen, S., van der Molen, J., de Mora, L., Polimene, L., Sailley, S., Stephens, N., Torres, R., 2016. ERSEM 15.06: A generic model for marine biogeochemistry and the ecosystem dynamics of the lower trophic levels. Geosci. Model Dev. 9, 1293–1339. https://doi.org/10.5194/gmd-9-1293-2016.
Catalá, T.S., Martínez-Pérez, A.M., Nieto-Cid, M., Álvarez, M., Otero, J., Emelianov, M., Reche, I., Arístegui, J., Álvarez-Salgado, X.A., 2018. Dissolved Organic Matter (DOM) in the open Mediterranean Sea. I. Basin–wide distribution and drivers of chromophoric DOM. Prog. Oceanogr. 165, 35–51. https://doi.org/10.1016/j.pocean.2018.05.002.
Catlett, D., Siegel, D.A., 2018. Phytoplankton Pigment Communities Can be Modeled Using Unique Relationships With Spectral Absorption Signatures in a Dynamic Coastal Environment. J. Geophys. Res. Oceans 123 (1), 246–264. https://doi.org/10.1002/2017JC013195.
Chisholm, S.W., 1992. In: Primary Productivity and Biogeochemical Cycles in the Sea. Springer US, Boston, MA, pp. 213–237. https://doi.org/10.1007/978-1-4899-0762-2_12.
Ciotti, Á.M., Lewis, M.R., Cullen, J.J., 2002. Assessment of the relationships between dominant cell size in natural phytoplankton communities and the spectral shape of the absorption coefficient. Limnol. Oceanogr. 47 (2), 404–417. https://doi.org/10.4319/lo.2002.47.2.0404.
Claustre, H., Morel, A., Hooker, S.B., Babin, M., Antoine, D., Oubelkheir, K., Bricaud, A., Leblanc, K., Quéguiner, B., Maritorena, S., 2002. Is desert dust making oligotrophic waters greener? Geophys. Res. Lett. 29 (10), 107-1–107-4. https://doi.org/10.1029/2001GL014056.
Clementson, L.A., Wojtasiewicz, B., 2019. Dataset on the in vivo absorption characteristics and pigment composition of various phytoplankton species. Data in brief 25, 104020. https://doi.org/10.1016/j.dib.2019.104020.
Cros, L., Fortuño, J.M., 2002. Atlas of Northwestern Mediterranean Coccolithophores. Scientia Marina 66 (S1), 1–182. https://doi.org/10.3989/scimar.2002.66s11.
Cunningham, B.R., Greenwold, M.J., Lachenmyer, E.M., Heidenreich, K.M., Davis, A.C., Dudycha, J.L., Richardson, T.L., Collier, J., 2019. Light capture and pigment diversity in marine and freshwater cryptophytes. J. Phycol. 55 (3), 552–564. https://doi.org/10.1111/jpy.12816.
D'Alimonte, D., Melin, F., Zibordi, G., Berthon, J.-F., 2003. Use of the novelty detection technique to identify the range of applicability of empirical ocean color algorithms. IEEE T Geosci. Remote 41 (12), 2833–2843. https://doi.org/10.1109/TGRS.2003.818020.
D'Alimonte, D., Zibordi, G., 2003. Phytoplankton determination in an optically complex coastal region using a multilayer perceptron neural network. IEEE T Geosci. Remote 41 (12), 2861–2868. https://doi.org/10.1109/TGRS.2003.817682.
Davies, E.J., Basedow, S.L., McKee, D., 2021. The hidden influence of large particles on ocean colour. Sci. Rep. 11 https://doi.org/10.1038/s41598-021-83610-5.
DiCicco, A., Sammartino, M., Marullo, S., Santoleri, R., 2017. Regional Empirical Algorithms for an Improved Identification of Phytoplankton Functional Types and Size Classes in the Mediterranean Sea Using Satellite Data. Front. Mar. Sci. 4, 126. https://doi.org/10.3389/fmars.2017.00126.
Dubinsky, Z., Falkowski, P.G., Wyman, K., 1986. Light harvesting and utilization by phytoplankton. Plant Cell Physiol. 27 (7), 1335–1349.
Dupouy, C., Neveux, J., Dirberg, G., Röttgers, R., Tenório, M.M.B., Ouillon, S., 2008. Bio-optical properties of the marine cyanobacteria Trichodesmium spp. J. Appl. Remote Sens. 2, 1–17. https://doi.org/10.1117/1.2839036.
Dutkiewicz, S., Hickman, A.E., Jahn, O., Gregg, W.W., Mouw, C.B., Follows, M.J., 2015. Capturing optically important constituents and properties in a marine biogeochemical and ecosystem model. Biogeosciences 12, 4447–4481. https://doi.org/10.5194/bg-12-4447-2015.
E.U. Copernicus Marine Service Information, 2020. Mediterranean Sea monthly reprocessed surface chlorophyll concentration from multi satellite observations + SeaWIFS daily climatology [WWW Document]. URL https://resources.marine.copernicus.eu/?option=com_csw&view=details&product_id=OCEANCOLOUR_MED_CHL_L4_REP_OBSERVATIONS_009_078 (accessed 6.30.20).
Fujiki, T., Taguchi, S., 2002. Variability in chlorophyll a specific absorption coefficient in marine phytoplankton as a function of cell size and irradiance. J Plank Res 24, 859–874. https://doi.org/10.1093/plankt/24.9.859.
Gallegos, C.L., Werdell, P.J., McClain, C.R., 2011. Long-term changes in light scattering in Chesapeake Bay inferred from Secchi depth, light attenuation, and remote sensing measurements. J. Geophys. Res. Oceans 116, 1–19. https://doi.org/10.1029/2011JC007160.
Geider, R.J., MacIntyre, H.L., Kana, T.M., 1997. Dynamic model of phytoplankton growth and acclimation: Responses of the balanced growth rate and the chlorophyll a:carbon ratio to light, nutrient-limitation and temperature. Mar. Ecol. Prog. Ser. 148, 187–200. https://doi.org/10.3354/meps148187.
Gentleman, W., Leising, A., Frost, B., Strom, S., Murray, J., 2003. Functional responses for zooplankton feeding on multiple resources: A review of assumptions and biological dynamics. Deep Sea Res PT II 50 (22-26), 2847–2875. https://doi.org/10.1016/j.dsr2.2003.07.001.
Gitelson, A., Karnieli, A., Goldman, N., Yacobi, Y.Z., Mayo, M., 1996. Chlorophyll estimation in the Southeastern Mediterranean using CZCS images: adaptation of an algorithm and its validation. J. Mar. Syst. 9 (3-4), 283–290. https://doi.org/10.1016/S0924-7963(95)00047-X.
Gregg, W.W., 2002. A Coupled Ocean–Atmosphere Radiative Model for Global Ocean Biogeochemical Model, NASA Technical Report Series on Global Modeling and Data Assimilation. NASA/TM- 2002-104606 22.
Gregg, W.W., Casey, N.W., 2009. Skill assessment of a spectral ocean-atmosphere radiative model. J. Mar. Syst. 76 (1-2), 49–63. https://doi.org/10.1016/j.jmarsys.2008.05.007.
Gregg, W.W., Rousseaux, C.S., 2017. Simulating PACE Global Ocean Radiances. Front. Mar. Sci. 4, 1–19. https://doi.org/10.3389/fmars.2017.00060.
Hickman, A.E., Dutkiewicz, S., Williams, R.G., Follows, M.J., 2010. Modelling the effects of chromatic adaptation on phytoplankton community structure in the oligotrophic ocean. Mar. Ecol. Prog. Ser. 406, 1–17. https://doi.org/10.3354/meps08588.
Hirata, T., Hardman-Mountford, N.J., Brewin, R.J.W., Aiken, J., Barlow, R., Suzuki, K., Isada, T., Howell, E., Hashioka, T., Noguchi-Aita, M., Yamanaka, Y., 2011. Synoptic relationships between surface Chlorophyll-a and diagnostic pigments specific to phytoplankton functional types. Biogeosciences 8, 311–327. https://doi.org/10.5194/bg-8-311-2011.
Holt, R.D., 1983. Optimal Foraging and the Form of the Predator Isocline. Am. Nat. 122 (4), 521–541.
Holt, R.D., 1977. Predation, Apparent Competition, and the Structure of Prey Communities. Theor. Popul Biol. 12 (2), 197–229.
Holtrop, T., Huisman, J., Stomp, M., Biersteker, L., Aerts, J., Grébert, T., Partensky, F., Garczarek, L., Woerd, H.J.V.D., 2021. Vibrational modes of water predict spectral niches for photosynthesis in lakes and oceans. Nat. Ecol. Evol. 5 (1), 55–66. https://doi.org/10.1038/s41559-020-01330-x.
Huisman, J., van Oostveen, P., Weissing, F.J., 1999. Species dynamics in phytoplankton blooms: Incomplete mixing and competition for light. Am. Nat. 154 (1), 46–68. https://doi.org/10.1086/303220.
Huisman, J., Weissing, F.J., 1995. Competition for nutrients and light in a mixed water column. Am. Nat. 146, 536–564. https://doi.org/10.1086/285814.
Huisman, J., Weissing, F.J., 1994. Light-limited growth and competition for light in well-mixed aquatic environments: An elementary model. Ecology 75, 507–520. https://doi.org/10.2307/1939554.
Ignatiades, L., Gotsis-Skretas, O., Pagou, K., Krasakopoulou, E., 2009. Diversification of phytoplankton community structure and related parameters along a large-scale longitudinal east-west transect of the Mediterranean Sea. J Plank Res 31, 411–428. https://doi.org/10.1093/plankt/fbn124.
Johnsen, G., Sakshaug, E., 2007. Biooptical characteristics of PSII and PSI in 33 species (13 pigment groups) of marine phytoplankton, and the relevance for pulse-amplitude-modulated and fast-repetition-rate fluorometry. J. Phycol. 43, 1236–1251. https://doi.org/10.1111/j.1529-8817.2007.00422.x.
Key, T., McCarthy, A., Campbell, D.A., Six, C., Roy, S., Finkel, Z.V., 2010. Cell size trade-offs govern light exploitation strategies in marine phytoplankton. Environ. Microbiol. 12, 95–104. https://doi.org/10.1111/j.1462-2920.2009.02046.x.
Kishino, M., Takahashi, M., Okami, N., Ichimura, S., 1985. Estimation of the spectral absorption coefficients of phytoplankton in the sea. Bull. Mar. Sci. 37, 634–642.
Kitidis, V., Stubbins, A.P., Uher, G., Upstill Goddard, R.C., Law, C.S., Woodward, E.M.S., 2006. Variability of chromophoric organic matter in surface waters of the Atlantic Ocean. Deep Sea Res PT II 53 (14-16), 1666–1684. https://doi.org/10.1016/j.dsr2.2006.05.009.
Krumhardt, K.M., Lovenduski, N.S., Iglesias-Rodriguez, M.D., Kleypas, J.A., 2017. Coccolithophore growth and calcification in a changing ocean. Prog. Oceanogr. 159, 276–295. https://doi.org/10.1016/j.pocean.2017.10.007.
Lazzari, P., Álvarez, E., Terzić, E., Cossarini, G., Chernov, I., D'Ortenzio, F., Organelli, E., 2021a. CDOM spatiotemporal variability in the Mediterranean Sea: a modelling study. J Mar Sci Eng 9. https://doi.org/10.3390/jmse9020176.
Lazzari, P., Salon, S., Terzić, E., Gregg, W.W., D'Ortenzio, F., Vellucci, V., Organelli, E., Antoine, D., 2021b. Assessment of the spectral downward irradiance at the surface of the Mediterranean Sea using the radiative Ocean-Atmosphere Spectral Irradiance Model (OASIM). Ocean Sci. 17, 675–697. https://doi.org/10.5194/os-17-675-2021.

Lazzari, P., Solidoro, C., Ibello, V., Salon, S., Teruzzi, A., Béranger, K., Colella, S., Crise, A., 2012. Seasonal and inter-annual variability of plankton chlorophyll and primary production in the Mediterranean Sea: A modelling approach. Biogeosciences 9 (1), 217–233. https://doi.org/10.5194/bg-9-217-201210.5194/bg-9-217-2012-supplement.

Lazzari, P., Solidoro, C., Salon, S., Bolzon, G., 2016. Spatial variability of phosphate and nitrate in the Mediterranean Sea: A modeling approach. Deep-Sea Res PT I 108, 39–52. https://doi.org/10.1016/j.dsr.2015.12.006.

Lazzari, P., Teruzzi, A., Salon, S., Campagna, S., Calonaci, C., Colella, S., Tonani, M., Crise, A., 2010. Pre-operational short-term forecasts for Mediterranean Sea biogeochemistry. Ocean Sci. 6 (1), 25–39. https://doi.org/10.5194/os-6-25-201010.5194/os-6-25-2010-supplement.

Lorenzo, M.R., Neale, P.J., Sobrino, C., León, P., Vázquez, V., Bresnan, E., Segovia, M., 2019. Effects of elevated CO2 on growth, calcification, and spectral dependence of photoinhibition in the coccolithophore Emiliania huxleyi (Prymnesiophyceae). J. Phycol. 55, 755–778. https://doi.org/10.1111/jpy.12885.

Luimstra, V.M., Verspagen, J.M.H., Xu, T., Schuurmans, J.M., Huisman, J., 2020. Changes in water color shift competition between phytoplankton species with contrasting light-harvesting strategies. Ecology 101 (3). https://doi.org/10.1002/ecy.2951.

Lutz, V.A., Sathyendaranath, S., Head, E.J.H., Li, W.K.W., 2001. Changes in the in vivo absorption and fluorescence excitation spectra with growth irradiance in three species of phytoplankton. J. Plankton Res. 23, 555–569. https://doi.org/10.1093/plankt/23.6.555.

Maechler, M., Rousseeuw, P., Struyf, A., Hubert, M., Hornik, K., 2019. cluster: Cluster Analysis Basics and Extensions. R package version 2 (1). https://CRAN.R-project.org/package=cluster.

Mao, Z., Stuart, V., Pan, D., Chen, J., Gong, F., Huang, H., Zhu, Q., 2010. Effects of phytoplankton species composition on absorption spectra and modeled hyperspectral reflectance. Ecol. Inf. 5 (5), 359–366. https://doi.org/10.1016/j.ecoinf.2010.04.004.

Metsamaa, L., Kutser, T., Strömbeck, N., 2006. Recognising cyanobacterial blooms based on their optical signature: a modeling study. Boreal Environmental Research 11, 493–506.

Mitchell, G., Kiefer, D.A., 1988. Chlorophyll a specific absorption and fluorescence excitation spectra for light-limited phytoplankton. Deep Sea Res 35, 639–663. https://doi.org/10.1016/0198-0149(88)90024-6.

Moberg, L., Karlberg, B., Sørensen, K., Källqvist, T., 2002. Assessment of phytoplankton class abundance using absorption spectra and chemometrics. Talanta 56, 153–160. https://doi.org/10.1016/S0039-9140(01)00555-0.

Moore, C.M., Lucas, M.I., Sanders, R., Davidson, R., 2005. Basin-scale variability of phytoplankton bio-optical characteristics in relation to bloom state and community structure in the Northeast Atlantic. Deep-Sea Res PT I 52 (3), 401–419. https://doi.org/10.1016/j.dsr.2004.09.003.

Moore, L.R., Chisholm, S.W., 1999. Photophysiology of the marine cyanobacterium Prochlorococcus: Ecotypic differences among cultured isolates. Limnol. Oceanogr. 44 (3), 628–638. https://doi.org/10.4319/lo.1999.44.3.0628.

Moore, L.R., Goericke, R., Chisholm, S.W., 1995. Comparative physiology of Synechococcus and Prochlorococcus: influence of light and temperature on growth, pigments, fluorescence and absorptive properties. Mar. Ecol. Prog. Ser. 116, 259–275.

Morel, A., 1987. Chlorophyll-specific scattering coefficient of phytoplankton. A simplified theoretical approach. Deep-Sea Res 34 (7), 1093–1105. https://doi.org/10.1016/0198-0149(87)90066-5.

Morel, A., 1974. Optical properties of pure water and pure sea water. In: Jerlov, N.G., Nielson, E.S. (Eds.), Optical Aspects of Oceanography. Academic Press, New York, pp. 1–24.

Morel, A., Ahn, Y.-H., Partensky, F., Vaulot, D., Claustre, H., 1993. Prochlorococcus and Synechococcus: A comparative study of their optical properties in relation to their size and pigmentation. J. Mar. Res. 51, 617–649. https://doi.org/10.1357/0022240933223963.

Morel, A., Bricaud, A., 1981. Theoretical results concerning light absorption in a discrete medium, and application to specific absorption of phytoplankton. Deep Sea Res 28 (11), 1375–1393. https://doi.org/10.1016/0198-0149(81)90039-X.

Mouriño-Carballido, B., Hojas, E., Cermeño, P., Chouciño, P., Fernández-Castro, B., Latasa, M., Marañón, E., Morán, X.A.G., Vidal, M., 2016. Nutrient supply controls picoplankton community structure during three contrasting seasons in the northwestern Mediterranean Sea. Mar. Ecol. Prog. Ser. 543, 1–19. https://doi.org/10.3354/meps11558.

Nair, A., 2007. Bio-optical properties of some phytoplankton functional types. Dalhousie University, Halifax, Nova Scotia. PhD thesis.

Organelli, E., Bricaud, A., Antoine, D., Matsuoka, A., 2014. Seasonal dynamics of light absorption by chromophoric dissolved organic matter (CDOM) in the NW Mediterranean Sea (BOUSSOLE site). Deep Sea Res. Part I: Oceanographic Research Papers 91, 72–85. https://doi.org/10.1016/j.dsr.2014.05.003.

Organelli, E., Nuccio, C., Lazzara, L., Uitz, J., Bricaud, A., Massi, L., 2017. On the discrimination of multiple phytoplankton groups from light absorption spectra of assemblages with mixed taxonomic composition and variable light conditions. Appl. Opt. 56 (14), 3952.

Organelli, E., Nuccio, C., Melillo, C., Massi, L., 2011. Relationships between phytoplankton light absorption, pigment composition and size structure in offshore areas of the Mediterranean Sea. Adv. Oceanogr. Limnol. 2 (2), 107–123. https://doi.org/10.1080/19475721.2011.607489.

Oviedo, A., Ziveri, P., Álvarez, M., Tanhua, T., 2015. Is coccolithophore distribution in the Mediterranean Sea related to seawater carbonate chemistry? Ocean Sci. 11, 13–32. https://doi.org/10.5194/os-11-13-2015.

Peloquin, J., Swan, C., Gruber, N., Vogt, M., Claustre, H., Ras, J., Uitz, J., Barlow, R., Behrenfeld, M., Bidigare, R., Dierssen, H., Ditullio, G., Fernandez, E., Gallienne, C., Gibb, S., Goericke, R., Harding, L., Head, E., Holligan, P., Hooker, S., Karl, D., Landry, M., Letelier, R., Llewellyn, C.A., Lomas, M., Lucas, M., Mannino, A., Marty, J.-C., Mitchell, B.G., Muller-Karger, F., Nelson, N., O'Brien, C., Prezelin, B., Repeta, D., Jr. Smith, W.O., Smythe-Wright, D., Stumpf, R., Subramaniam, A., Suzuki, K., Trees, C., Vernet, M., Wasmund, N., Wright, S., 2013. The MAREDAT global database of high performance liquid chromatography marine pigment measurements. Earth Syst. Sci. Data 5 (1), 109–123. https://doi.org/10.5194/essd-5-109-2013.

Pérez, G.L., Galí, M., Royer, S.-J., Gerea, M., Ortega-Retuerta, E., Gasol, J.M., Marrasé, C., Simó, R., 2021. Variability of phytoplankton light absorption in stratified waters of the NW Mediterranean Sea: The interplay between pigment composition and the packaging effect. Deep Sea Res PT 169, 103460. https://doi.org/10.1016/j.dsr.2020.103460.

Poisot, T., 2011. The digitize Package: Extracting Numerical Data from Scatterplots. The R Journal 3, 25–26. https://doi.org/10.32614/RJ-2011-004.

Pope, R.M., Fry, E.S., 1997. Absorption spectrum 380–700 nm of pure water. II. Integrating cavity measurements. Appl. Optics 36 (33), 8710. https://doi.org/10.1364/AO.36.008710.

Proctor, C.W., Roesler, C.S., 2010. New insights on obtaining phytoplankton concentration and composition from in situ multispectral chlorophyll fluorescence. Limnol Oceanogr Meth 8, 695–708. https://doi.org/10.4319/lom.2010.8.695.

Prowe, A.E.F., Pahlow, M., Dutkiewicz, S., Follows, M., Oschlies, A., 2012. Top-down control of marine phytoplankton diversity in a global ecosystem model. Prog. Oceanogr. 101 (1), 1–13. https://doi.org/10.1016/j.pocean.2011.11.016.

R Core Team, 2020. R: A language and environment for statistical computing. R Foundation for Statistical Computing, Vienna, Austria https://www.R-project.org/.

Salon, S., Cossarini, G., Bolzon, G., Feudale, L., Lazzari, P., Teruzzi, A., Solidoro, C., Crise, A., 2019. Novel metrics based on biogeochemical argo data to improve the model uncertainty evaluation of the cmems mediterranean marine ecosystem forecasts. Ocean Sci. 15, 997–1022. https://doi.org/10.5194/os-15-997-2019.

Sathyendranath, S., Lazzara, L., Prieur, L., 1987. Variations in the spectral values of specific absorption of phytoplankton. Limnol. Oceanogr. 32 (2), 403–415. https://doi.org/10.4319/lo.1987.32.2.0403.

Sauer, M.J., Roesler, C.S., Werdell, P.J., Barnard, A., 2012. Under the hood of satellite empirical chlorophyll a algorithms: revealing the dependencies of maximum band ratio algorithms on inherent optical properties. Opt. Express 20, 20920–20933. https://doi.org/10.1364/OE.20.020920.

Siokou-Frangou, I., Christaki, U., Mazzocchi, M.G., Montresor, M., Ribera d'Alcalá, M., Vaqué, D., Zingone, A., Comunale, V., 2010. Plankton in the open Mediterranean Sea: a review. Biogeosciences 7, 1543–1586. https://doi.org/10.5194/bg-7-1543-2010.

Six, C., Finkel, Z.V., Irwin, A.J., Campbell, D.A., Thompson, R., 2007. Light variability illuminates niche-partitioning among marine picocyanobacteria. PLoS ONE 2 (12), e1341. https://doi.org/10.1371/journal.pone.0001341.

Smith, R.C., Baker, K.S., 1981. Optical properties of the clearest natural waters (200–800 nm). Appl. Opt. 20, 177–184. https://doi.org/10.1364/AO.20.000177.

Staehr, P.A., Henriksen, P., Markager, S., 2002. Photoacclimation of four marine phytoplankton species to irradiance and nutrient availability. Mar. Ecol. Prog. Ser. 238, 47–59. https://doi.org/10.3354/meps238047.

Stomp, M., Huisman, J., de Jongh, F., Veraart, A.J., Gerla, D., Rijkeboer, M., Ibelings, B. W., Wollenzien, U.I.A., Stal, L.J., 2004. Adaptive divergence in pigment composition promotes phytoplankton biodiversity. Nature 432 (7013), 104–107. https://doi.org/10.1038/nature03044.

Stomp, M., Huisman, J., Vörös, L., Pick, F.R., Laamanen, M., Haverkamp, T., Stal, L.J., 2007. Colourful coexistence of red and green picocyanobacteria in lakes and seas. Ecol. Lett. 10 (4), 290–298. https://doi.org/10.1111/j.1461-0248.2007.01026.x.

Stramski, D., Kiefer, D.A., 1998. Can heterotrophic bacteria be important to marine light absorption? J. Plankton Res. 20 (8), 1489–1500. https://doi.org/10.1093/plankt/20.8.1489.

Stramski, D., Morel, A., 1990. Optical properties of photosynthetic picoplankton in different physiological states as affected by growth irradiance. Deep Sea Res 37 (2), 245–266. https://doi.org/10.1016/0198-0149(90)90126-G.

Subramaniam, A., Carpenter, E.J., Falkowski, P.G., 1999. Bio-optical properties of the marine diazotrophic cyanobacteria Trichodesmium spp. II. A reflectance model for remote sensing. Limnol. Oceanogr. 44 (3), 618–627. https://doi.org/10.4319/lo.1999.44.3.0618.

Suggett, D.J., Le Floc'H, E., Harris, G.N., Leonardos, N., Geider, R.J., 2007. Different strategies of photoacclimation by two strains of Emiliania huxleyi (Haptophyta). J. Phycol. 43, 1209–1222. https://doi.org/10.1111/j.1529-8817.2007.00406.x.

Suggett, D.J., MacIntyre, H.L., Geider, R.J., 2004. Evaluation of biophysical and optical determinations of light absorption by photosystem II in phytoplankton. Limnol Oceanogr Meth 2 (10), 316–332. https://doi.org/10.4319/lom.2004.2.316.

Terzić, E., Miró, A., Organelli, E., Kowalczuk, P., D'Ortenzio, F., Lazzari, P., 2021. Radiative transfer modeling with Biogeochemical-Argo float data in the Mediterranean Sea. J. Geophys. Res. Oceans 126. https://doi.org/10.1029/2021JC017690.

Torrecilla, E., Stramski, D., Reynolds, R.A., Millán-Núñez, E., Piera, J., 2011. Cluster analysis of hyperspectral optical data for discriminating phytoplankton pigment assemblages in the open ocean. Remote Sens. Environ. 115 (10), 2578–2593. https://doi.org/10.1016/j.rse.2011.05.014.

Turley, C.M., Bianchi, M., Christaki, U., Conan, P., Harris, JRW, Psarra, S., Ruddy, G., Stutt, E.D., Tselepides, A., Van Wambeke, F., 2000. Relationship between primary producers and bacteria in an oligotrophic sea-the Mediterranean and biogeochemical

implications. Mar. Ecol. Prog. Ser. 193, 11–18. https://doi.org/10.3354/meps193011.
Uitz, J., Claustre, H., Morel, A., Hooker, S.B., 2006. Vertical distribution of phytoplankton communities in open ocean: An assessment based on surface chlorophyll. J. Geophys. Res. 111 (C8) https://doi.org/10.1029/2005JC003207.
Uitz, J., Stramski, D., Reynolds, R.A., Dubranna, J., 2015. Assessing phytoplankton community composition from hyperspectral measurements of phytoplankton absorption coefficient and remote-sensing reflectance in open-ocean environments. Remote Sens. Environ. 171, 58–74. https://doi.org/10.1016/j.rse.2015.09.027.
Vallina, S.M., Ward, B.A., Dutkiewicz, S., Follows, M.J., 2014. Maximal feeding with active prey-switching: A kill-the-winner functional response and its effect on global diversity and biogeography. Prog. Oceanogr. 120, 93–109. https://doi.org/10.1016/j.pocean.2013.08.001.
Vichi, M., Lovato, T., Lazzari, P., Cossarini, G., Gutierrez Mlot, E., Mattia, G., Masina, S., McKiver, W.J., Pinardi, N., Solidoro, C., Tedesco, L., Zavatarelli, M., 2015. The Biogeochemical Flux Model (BFM). Equation Description and User Manual.
Vichi, M., Pinardi, N., Masina, S., 2007. A generalized model of pelagic biogeochemistry for the global ocean ecosystem. Part I: Theory. J. Mar. Syst. 64 (1-4), 89–109. https://doi.org/10.1016/j.jmarsys.2006.03.006.
Vichi, M., Ruardij, P., Baretta, J.W., 2004. Link or sink: a modelling interpretation of the open Baltic biogeochemistry. Biogeosciences 1 (1), 79–100. https://doi.org/10.5194/bg-1-79-200410.5194/bg-1-79-2004-supplement.
Vidussi, F., Claustre, H., Manca, B.B., Luchetta, A., Marty, J.-C., 2001. Phytoplankton pigment distribution in relation to upper thermocline circulation in the eastern Mediterranean Sea during winter. J. Geophys. Res. Oceans 106 (C9), 19939–19956.
Visser, A.W., Fiksen, Ø., 2013. Optimal foraging in marine ecosystem models: selectivity, profitability and switching. Mar. Ecol. Prog. Ser. 473, 91–101. https://doi.org/10.3354/meps10079.
Volpe, G., Colella, S., Brando, V.E., Forneris, V., La Padula, F., Di Cicco, A., Sammartino, M., Bracaglia, M., Artuso, F., Santoleri, R., 2019. Mediterranean ocean colour Level 3 operational multi-sensor processing. Ocean Sci. 15 (1), 127–146. https://doi.org/10.5194/os-15-127-2019.
Volpe, G., Santoleri, R., Vellucci, V., Ribera d'Alcalà, M., Marullo, S., D'Ortenzio, F., 2007. The colour of the Mediterranean Sea: Global versus regional bio-optical algorithms evaluation and implication for satellite chlorophyll estimates. Remote Sens. Environ. 107 (4), 625–638. https://doi.org/10.1016/j.rse.2006.10.017.
Wagner, S., Schubotz, F., Kaiser, K., Hallmann, C., Waska, H., Rossel, P.E., Hansman, R., Elvert, M., Middelburg, J.J., Engel, A., Blattmann, T.M., Catalá, T.S., Lennartz, S.T., Gomez-Saez, G.V., Pantoja-Gutiérrez, S., Bao, R., Galy, V., 2020. Soothsaying DOM: A Current Perspective on the Future of Oceanic Dissolved Organic Carbon. Front. Marine Sci. 7 https://doi.org/10.3389/fmars.2020.00341.
Webb, W.L., Newton, M., Starr, D., 1974. Carbon dioxide exchange of Alnus rubra: a mathematical model. Oecologia 17 (4), 281–291. https://doi.org/10.1007/BF00345747.
Whitmire L, A, Pegau Scott, W, Karp-Boss, L, Boss, E, Cowles J, T, 2010. Spectral backscattering properties of marine phytoplankton cultures. Opt. Express 18 (14), 15073–15093. https://doi.org/10.1364/OE.18.015073.
Wojtasiewicz, B., Stoń-Egiert, J., 2016. Bio-optical characterization of selected cyanobacteria strains present in marine and freshwater ecosystems. J. Appl. Phycol. 28 (4), 2299–2314. https://doi.org/10.1007/s10811-015-0774-3.
Xi, H., Hieronymi, M., Krasemann, H., Röttgers, R., 2017. Phytoplankton Group Identification Using Simulated and In situ Hyperspectral Remote Sensing Reflectance. Front. Mar. Sci. 4, 272. https://doi.org/10.3389/fmars.2017.00272.
Xi, H., Hieronymi, M., Röttgers, R., Krasemann, H., Qiu, Z., 2015. Hyperspectral differentiation of phytoplankton taxonomic groups: a comparison between using remote sensing reflectance and absorption spectra. Remote Sens. 7, 14781–14805. https://doi.org/10.3390/rs71114781.
Xiu, P., Chai, F., 2014. Connections between physical, optical and biogeochemical processes in the Pacific Ocean. Prog. Oceanogr. 122, 30–53. https://doi.org/10.1016/j.pocean.2013.11.008.
Yacobi, Y.Z., Zohary, T., Kress, N., Hecht, A., Robarts, R.D., Waiser, M., Wood, A.M., Li, W.K.W., 1995. Chlorophyll distribution throughout the southeastern Mediterranean in relation to the physical structure of the water mass. J. Mar. Syst. 6 (3), 179–190. https://doi.org/10.1016/0924-7963(94)00028-A.
Zhou, W., Wang, G., Sun, Z., Cao, W., Xu, Z., Hu, S., Zhao, J., 2012. Variations in the optical scattering properties of phytoplankton cultures. Opt. Express 20, 11189–11206. https://doi.org/10.1364/OE.20.011189.